

MAXSS:

Algorithm Theoretical Baseline Document for SFMR-based Satellite-derived Extreme Wind Recalibration

(ATBD)

Doc. No.: Xxx

Issue. No.: 1.0

Version: 2.0.0

Date: 22 June 2022

Document prepared under ESA Contract Number: 4000132954/20/I-NB

Table of contents

1	Introduction.....	3
1.1	Study objective	4
1.2	Document objective and organisation.....	4
1.3	Applicable and reference documents.....	5
2	SFMR-Satellite collocation methodology.....	5
2.1	Datasets	5
2.2	Collocation procedure	7
3	Spatial resolution effects	11
4	Quality control effects.....	15
4.1	C-band scatterometer QC.....	15
4.2	Ku-band scatterometer QC.....	16
4.3	Radiometer QC.....	17
5	SFMR calibration effects.....	21
6	Scatterometer recalibration	22
6.1	C-band systems	22
6.2	Ku-band systems	26
7	Radiometer recalibration	31
7.1	AMSR-2	32
7.2	Windsat.....	34
7.3	SMAP.....	37
7.4	SMOS.....	39
8	REFERENCES	41

1 INTRODUCTION

A prerequisite for a successful development of the multi-mission wind (MMW) product is to ensure good inter-calibration of the different extreme wind datasets to be integrated in the product. Since the operational hurricane community is working with the in-situ dropsondes as wind speed reference, which are in turn used to calibrate the NOAA Hurricane Hunter Stepped Frequency Microwave Radiometer (SFMR) wind data (Uhlhorn et al., 2007), MAXSS uses the latter to ensure inter-calibration among the Tier-1 medium-resolution swath-based scatterometer and radiometer systems described in Section 2.2 and listed in Tables 1 and 2 of [MAXSS Team, 2021]. In short, these are: the Advanced Scatterometers onboard the Metop series (i.e., ASCAT-A, -B, and -C), the scatterometers onboard Oceansat-2 (OSCAT) and ScatSat-1 (OSCAT-2), and onboard the HY-2 series (HSCAT-A, -B); the Advanced Microwave Scanning Radiometer 2 onboard GCOM-W1 (AMSR-2), the multi-frequency polarimetric radiometer (Windsat), and the L-band radiometers onboard the Soil Moisture and Ocean Salinity (SMOS) and the Soil Moisture Active Passive (SMAP) missions.

Within the SMOS+STORM [Reul et al., 2017] and CHEFS [Stoffelen et al., 2020] projects, a preliminary calibration of, respectively, SMOS and ASCAT-A extreme winds has been carried out, using a long time series of collocated satellite-SFMR wind data in storm-centric coordinates, which are based on Best Track data. In particular, in the framework of CHEFS, SFMR winds are upscaled to account for ASCAT-A resolved spatial scales (or representativeness), and then used as reference for ASCAT wind recalibration purposes. The so-called ASCAT dropsonde-scale winds show sensitivity to high winds, and an overall correlation with SFMR upscaled winds of about 0.9 [Polverari et al., 2022]. The saturation of the GMF at extreme winds is somehow compensated by the high calibration stability of the ASCAT-A instrument. This SFMR-based re-calibration approach is revisited in MAXSS and applied to all the mentioned medium-resolution scatterometer and radiometer systems to ensure extreme wind inter-calibration of such systems.

Note that several sources of collocation errors have been reported, namely the Best Track temporal sampling and geolocation inaccuracies and the temporal differences between the SFMR and scatterometer acquisitions [Stoffelen et al., 2020]. However, mission-long datarecords are collocated with SFMR in order to mitigate the effect of collocation errors in the recalibration process. Moreover, the assumption of proper inter-calibration among satellite winds from the same data provider (i.e., the Ocean and Sea Ice Satellite Application Facility or OSI SAF for scatterometers and the Remote Sensing Systems or REMSS for all radiometers but SMOS) is used to improve the recalibration fit.

Regarding spatial representativeness, since the different extreme wind systems resolve different spatial scales, a different SFMR upscaling procedure (i.e., along-track averaging) is applied to each system.

The impact of quality control (QC) and, in particular, rain contamination in the calibration fit is analysed. Special attention is drawn to analyse rain effects on the winds derived from Ku-band scatterometers and higher frequency radiometers (Windsat and AMSR-E).

Also relevant, SFMR calibration is found to change over time, in the period 2009-2020. This poses a few challenges in the SFMR-based recalibration procedure, which are addressed in this report.

Note that the differences between the extreme wind gradient tropical cyclone (TC) regions and the relatively lower wind gradient extra-tropical TC (ETC) regions were initially planned to be analyzed in order to further tune the extreme wind scaling for each system. However, the SFMR wind datasets over ETCs have not yet been released by NOAA since they are still analyzing the relevant differences between SFMR TC and ETC retrievals. No SFMR ETC wind data will be released until they reprocess the entire ETC dataset and get a better handle on the mentioned differences (personal communication with Joe Sapp, Zorana Jelenak, and Paul Chang, NOAA-NESDIS).

As such, a two-step strategy has been finally implemented to recalibrate the high and extreme wind speeds derived from the mentioned scatterometer and radiometer systems in the period 2009-2020. First, the C-band ASCATs have been recalibrated against collocated storm-motion centric SFMR wind data. Then, both SFMR winds and ASCAT recalibrated winds have been used to recalibrate all the other satellite wind systems. In doing so, a good inter-calibration between all the systems is ensured not only under TC conditions, but also elsewhere.

1.1 Study objective

The aims of this study are to recalibrate scatterometer- and radiometer-derived high and extreme winds using collocated NOAA hurricane hunter Stepped Frequency Microwave Radiometer (SFMR) winds as reference, and to ensure a good inter-calibration of all the mentioned satellite wind sources, which will be used as input to the MAXSS multi-mission wind product generation.

1.2 Document objective and organisation

This document describes the satellite-SFMR collocation and calibration methodologies, as well as, the spatial representativeness, quality control, and SFMR calibration effects on the

recalibration procedure. In Section 2, the satellite, SFMR, and Best Track datasets are briefly presented, and the satellite-SFMR collocation methodology is described. Sections 3-5 present an analysis on spatial representation, quality control, and SFMR calibration effects, respectively. Finally, in Sections 6 and 7, the scatterometer and radiometer extreme wind recalibration methodology is presented, implemented, and verified.

1.3 Applicable and reference documents

[MAXSS Team, 2021] Bonekamp et al., "MAXSS Requirements Baseline", 4000132954/20/I-NB D1, MAXSS-RB012, Technical report v012, October 2021.

2 SFMR-SATELLITE COLLOCATION METHODOLOGY

2.1 Datasets

a) Satellite data

A short description of the Tier-1 medium-resolution swath-based active and passive systems described in Section 2.2 of [MAXSS Team, 2021] is provided below:

- OSI SAF Level 2 12.5-km ASCAT-A, -B and -C wind products, reprocessed with the Eumetsat Numerical Weather Prediction Satellite Application Facility (NWP-SAF) ASCAT Wind Data Processor (AWDP) version 3.3, using CMOD7 Geophysical Model Function (GMF) [Stoffelen et al., 2017] and collocated ERA5 stress-equivalent winds (U10S) [De Kloe et al., 2017] as background wind for ambiguity removal (AR) purposes, for the periods 01/2009-12/2020, 11/2012-12/2020, and 01/2019-12/2020, respectively.
- OSI SAF Level 2 25-km OSCAT (onboard Oceansat-2), HSCAT-A (onboard HY-2A), RapidScat, OSCAT-2 (onboard Scatsat-1), and HSCAT-B (onboard HY-2B), reprocessed with the NWP-SAF Pencil-beam Wind Processor (PenWP) version 2.2, using NSCAT-4DS GMF [Wang et al., 2017] and collocated ERA5 U10S as background wind for AR purposes, for the periods 01/2010-02/2014, 06/2012-04/2015, 11/2014-08/2016, 01/2017-12/2020, 01/2019-12/2020, respectively.

- REMSS Level 3 daily 0.25 deg All Weather (AW) AMSR-2 version 8.2, AW Windsat version 7.0.1, and SMAP version 1.0 near-surface wind products, for the periods 07/2012-12/2020, 01/2010-10/2020, and 04/2015-12/2020, respectively, available from <https://www.remss.com/missions/>.
- Ifremer Level 2 0.25 deg SMOS wind product version 2.0, for the period 01/2010-12/2020, available from ftp://ftp.ifremer.fr/ifremer/cersat/users/cprevost/smoswindv2_repro/not_validate_d/12/.

Note that there exists an AMSR-2 and a Windsat wind product specifically developed for TC conditions, the so-called TC wind products. However, such products do not contain wind information (i.e., wind speed set to missing), for cold waters ($SST < 20^{\circ}\text{C}$) or low winds (wind speed < 10 m/s). Since for MAXSS, global wind coverage is required, the REMSS all-weather (AW) AMSR-2 and Windsat wind products are used instead. Note also that the quality of AMSR-2 AW version 8.2 winds is comparable to that of the AMSR-2 TC winds, for rain rates below 12 mm/h. However, the Windsat AW version 8 wind product is currently under development [Meissner et al, 2021], [Manaster et al., 2021], and is expected to be delivered later this year. As such, the current Windsat AW version 7.0.1 wind product is used, the development of which has not specifically considered TC winds (personal communication with Thomas Meissner and Lucrezia Ricciardulli, REMSS).

b) SFMR data

The SFMR datasets for the period 2009-2020 are provided by the NOAA/NESDIS/STAR Ocean Surface Wind Team (OSWT). These datasets have been acquired by the many NOAA WP-3D and U.S. Air Force Reserve Command (AFRC) flights over several hurricane seasons. For each flight, a hurricane hunter aircraft crosses the storm centre several times, acquiring both SFMR sea surface wind and rain along with wind profiles from the Global Positioning System (GPS) dropsondes. An example of the SFMR wind speed variation along a flight trajectory is shown in Figure 1. As can be seen from the SFMR wind variation, during each storm cross, the wind intensity alternatively goes from high to low speeds and the wind minima usually move during this time, identifying the movement of the storm.

The NOAA/NESDIS/STAR OSWT has reprocessed the SFMR dataset by using a new version of their GMF that corrects an approximate 10% low bias observed in the SFMR wind retrievals with respect to dropsondes, for winds ranging between 15 m/s and 45 m/s [Sapp et al., 2019]. As mentioned in [Koltz and Ulhorn, 2014], [Sapp et al., 2019], the validity of the SFMR low wind speeds (< 15 m/s) and low rain rate (< 10 mm/h) are questionable due to the sensitivity of the instrument to physical processes that need to be better understood. Further details on the SFMR processing are provided in Section 2.2.7 of [MAXSS Team, 2021].

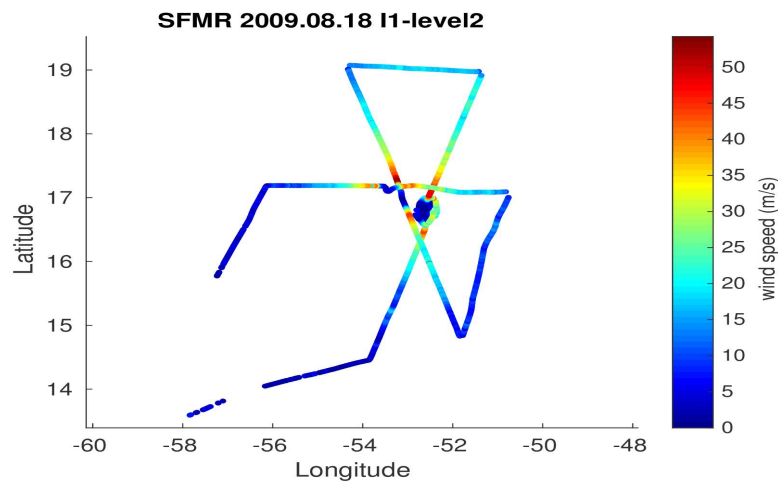


Figure 1. SFMR sea surface wind speed variation during the NOAA hurricane hunters flight experiment on August 18th, 2009.

c) Best Track data

The TC “Best Track” (hereafter BT) data obtained from the WMO International Best Track Archive for Climate Stewardship (IBTrACS) [Knapp et al., 2010] are used in this study in order to locate the storm center as sampled by each ASCAT overpass. In particular, we used the BT data set version v04r00, available at the NOAA National Climate Data Center (<https://www.ncdc.noaa.gov/ibtracs/>). The BT data sets provide an estimate of the storm position every three hours for the whole duration of the storm. We carried out a linear interpolation in order to have a BT storm position every second (hereafter BTsec position) in line with the SFMR temporal sampling rate. The wind community still argues about the accuracy of the BT center estimates, notably when interpolated in between 3-hour periods. But, so far, the BT data set is the only source publicly available online, providing the storm positions for most of the storm duration.

2.2 Collocation procedure

Following [Polverari et al., 2022], the satellite-derived winds are collocated with SFMR winds by using SFMR storm-motion centric coordinates to allow collocations even when they are separated by a few hours in time. The underlying assumption is that within a certain temporal window (e.g., 2 or 3 hours), the hurricane structure does not change with respect to the direction of the storm displacement. As such, SFMR spatially and temporally varying observations are projected into a “frozen” hurricane structure during such temporal window. This is done by converting the SFMR coordinates into a new coordinate system identified by the BT position at the time of each SFMR sample.

Different options can be considered for the new coordinate system reference (i.e., the storm motion direction). One option is to use the motion vector derived from consecutive BTsec points at every SFMR (1-sec) sampled location. Note that BT data are three hours apart, meaning that all SFMR acquisitions within such time frame share the same storm motion vector. Although such option seems quite consistent since the conversion closely follows the storm track as seen by the BT data, it may cause artefacts when the SFMR flight occurs over two consecutive BT 3-hour periods and there is a significant change of the storm motion direction. Alternatively, one can use splines to smoothly interpolate over the BT 3-hour positions, however, the exact storm motion turn within the 3-hour period is unknown, which means that any interpolation strategy would lead to storm motion vector errors.

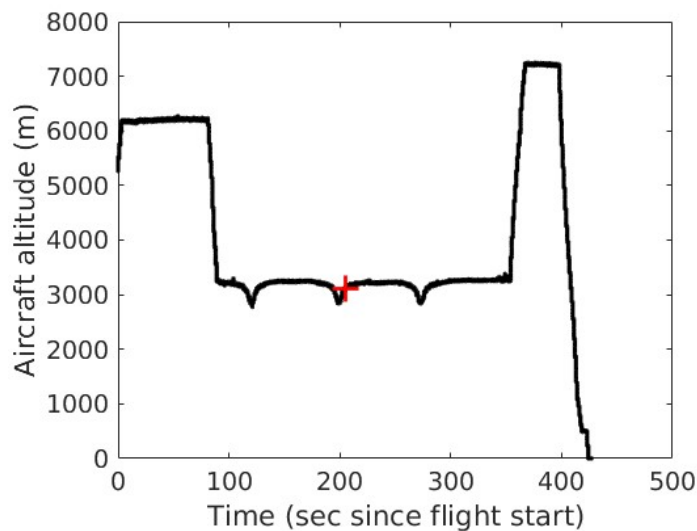


Figure 2. NOAA flight SFMR170903H1 during Hurricane Irma on September 3rd, 2017. Aircraft altitude with respect to time, along with the altitude at t_{mean}^{SFMR} (red cross), the portion of the flight around 3 km corresponds to the aircraft storm-crossing operation (adopted from [Polverari et al., 2022]).

A more practical approach to avoid such artefacts is to use a single vector, which best represents the storm motion at the time of the SFMR flight or the satellite overpass. In this analysis, the BTsec position at the time corresponding to the middle of the temporal window over which the aircraft crosses the storm (t_{mean}^{SFMR}), is used to compute the single storm motion vector. The t_{mean}^{SFMR} value has been computed by using the mean time of the SFMR wind speed measurements within the highest 15% wind speed data. To validate this time value, the aircraft altitude has been used. In particular, during the storm crossings operation, the aircraft altitude is relatively constant, so that t_{mean}^{SFMR} can be seen as the time in the middle of the temporal window in which the aircraft stays at such operational altitude. An example of the typical aircraft altitude and the corresponding t_{mean}^{SFMR} is shown in Figure 2. Once the BT

position at t_{mean}^{SFMR} has been identified, the corresponding storm motion vector is selected as reference vector and used to convert the SFMR trajectory such that each SFMR point is referenced to the storm centre in polar coordinates. Figures 3a and 3b show an example of the trajectory of the NOAA flight H1 during Hurricane Irma on September 3rd, 2017, in its original coordinates and in polar storm-motion relative coordinates, respectively.

It is important to mention that, due to the large variety of storm cases, the selected t_{mean}^{SFMR} may sometimes correspond either to the beginning or to the end of the storm crossing time window, depending on how strong the winds are within each cross. In the cases in which the SFMR storm centre crossings are within two different BT 3-hour windows, different t_{mean}^{SFMR} estimation approaches may lead to either one storm motion vector or another. However, the use of one vector with respect to another, if close in time, does not significantly affect the results, since both are equally (un)certain. The main limitation of this methodology is that, besides the uncertainty in the BT data itself, the storm track is unknown within the three hours separating two BT points. As a consequence, the selected reference vector may not accurately describe the actual storm movement, especially if the storm rapidly changes during this time. We assume that the storm velocity is constant over the 3-hour period, which can be a rather crude assumption.

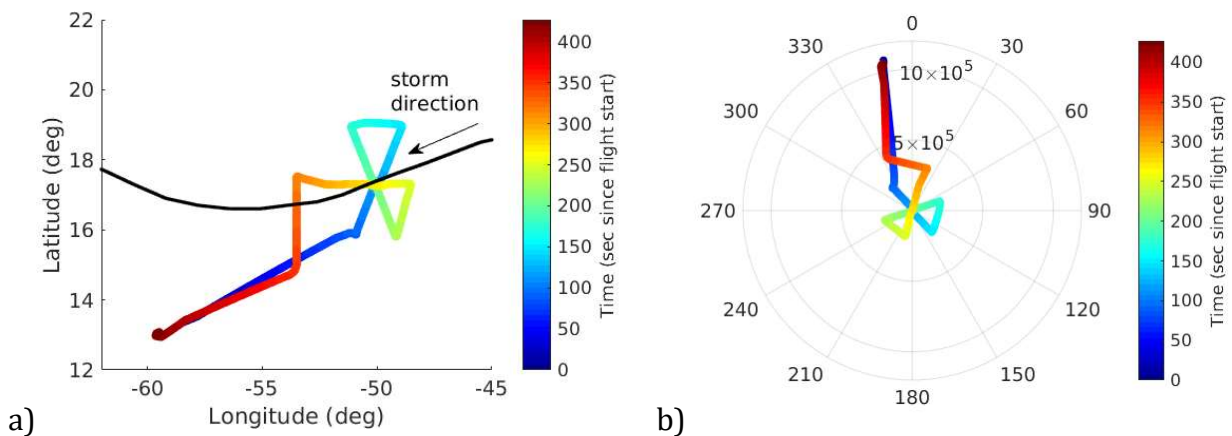


Figure 3. NOAA flight SFMR170903H1 during Hurricane Irma on September 3rd, 2017. (a) Aircraft trajectory in original coordinates with respect to time (see colorbar), along with the BT data (black line); (b) Corresponding flight in storm-motion relative coordinates (adopted from [Polverari et al., 2022]).

The converted SFMR trajectory is then relocated and centered on the BTsec position at the time of the satellite pass (t_{SAT}^C). The satellite storm center and the corresponding BTsec point are selected as the satellite wind vector cell (WVC) / BTsec pair having no time difference (i.e., zero seconds), and minimum spatial distance no larger than WVC grid size/ $\sqrt{2}$ km. [Note that for those satellite products providing the acquisition time in minutes (i.e., Windsat and SMAP),

the latter is converted to seconds for consistency with the other satellite products]. When the satellite pass does not catch the whole storm structure and, in turn, the BTsec point is out of the satellite swath, the selected WVC is the one having spatial distance less than 200 km. The SFMR storm-motion centric polar coordinates are then converted into latitudes/longitudes by using the reference motion vector corresponding to the BTsec at t_{SAT}^C . Figure 4a shows the ASCAT-A wind field over Hurricane Karl on September 23rd, 2016 along with the storm BTsec positions within a few hours from the ASCAT-A pass (purple line). The black lines in Figures 3a and 3b correspond to the NOAA I2 SFMR flight trajectory in original and storm-motion relative coordinates, respectively.

Note that, the assumption on the “frozen” hurricane structure cannot hold for long time differences. Therefore, the time separation Δt between each SFMR wind acquisition and the satellite pass, as defined in (1), is taken into account to carry out the wind comparison:

$$\Delta t = |t_{SAT}^C - t_i^{SFMR}| \quad (1)$$

where t_i^{SFMR} is the time of the collocated SFMR measurements. [Polverari et al., 2022] assess the Δt impact on the wind comparison by carrying out an ASCAT-A/SFMR wind difference analysis at different Δt values, i.e., $\Delta t \leq 1$ h, $\Delta t \leq 2$ h, $\Delta t \leq 3$ h. As expected, the scatter increases with Δt , but the increase is relatively moderate, with a standard deviation between 4.18-4.38 m/s. In addition, ASCAT-A and SFMR are very well correlated, with a correlation coefficient of about 0.88, showing that the hurricane frozen structure assumption holds reasonably well when there is a statistically significant number of collocations. In MAXSS, we use mostly mission-long datarecords and a $\Delta t \leq 3$ h in order to maximize the satellite-SFMR collocations.

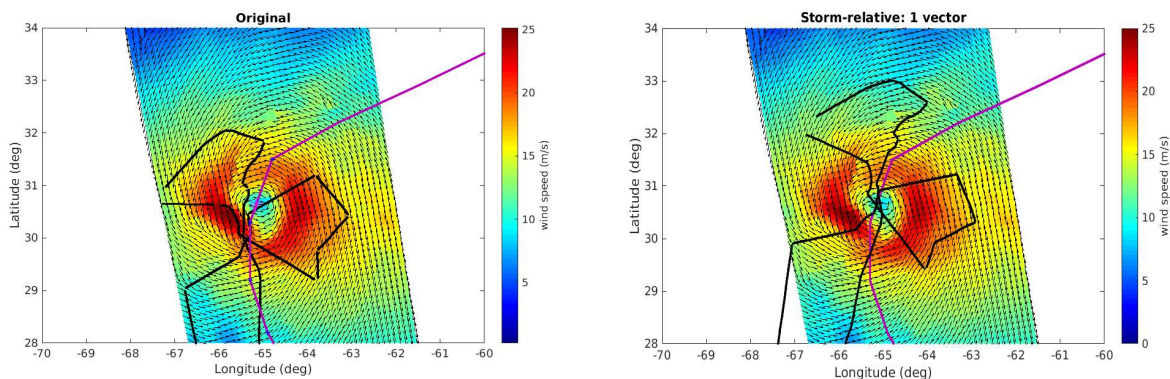


Figure 4. ASCAT wind field over Hurricane Karl on September 23rd, 2016 along with the storm BTsec positions within a few hours from the ASCAT-A pass (purple line). The black line corresponds to the NOAA I2 SFMR flight trajectory in original coordinates (a), and the storm-motion relative coordinates derived using a single vector (b) (adopted from [Polverari et al., 2022]).

3 SPATIAL RESOLUTION EFFECTS

The different extreme wind sensing systems used in this study resolve different spatial scales. This difference is particularly relevant in areas of high wind gradients, as those close to the TC eyewall. In order to address the representativeness differences between SFMR and satellite winds, the impact of SFMR upscaling in our wind comparisons is thoroughly analysed.

Figure 5 shows a comparison between SFMR winds at the original resolution (i.e., the non averaged product) and several collocated SFMR along-track averaged winds. The averaging is computed for temporal windows (centered at the non-averaged SFMR position) of 101 sec, 201 sec, 301 sec, and 401 sec. Assuming that the aircraft speed is 100 m/s on average, such temporal distances correspond to a spatial distance of 10 km, 20 km, 30 km, and 40 km, respectively. Note that, while performing SFMR averagings, only those 1D averaged tracks with at least 80% of valid wind points are used. Also, 1D averaged tracks including aircraft significant turns (such as those in between flight legs) are discarded.

Note that, as expected, the along-track averaged winds underestimate the most extreme SFMR winds, and this underestimation increases with along-track averaged distance. Likewise, the along-track averaged winds overestimate the relatively low winds away from the eyewall (e.g., close to the storm centre). This shows the impact of spatial resolution on how well the steepest wind gradient regions are resolved.

Figure 6a shows an example of an SFMR flight leg across Hurricane Matthew. As expected, the longer the SFMR averaging is, the less well-resolved is the TC eyewall structure. Figure 6b shows the same as Figure 6a but only for those SFMR points collocated with ASCAT-A (i.e., at 12.5 km subsampling). It is clear that the eyewall structure is not well resolved by any of the SFMR products (incl. the non-averaged product) due to the 12.5 km subsampling. Moreover, the spatial resolution effect is less pronounced because of the sampling, i.e., the peak winds and the peak wind differences between the coloured curves are significantly smaller in Figure 6b than in Figure 6a.

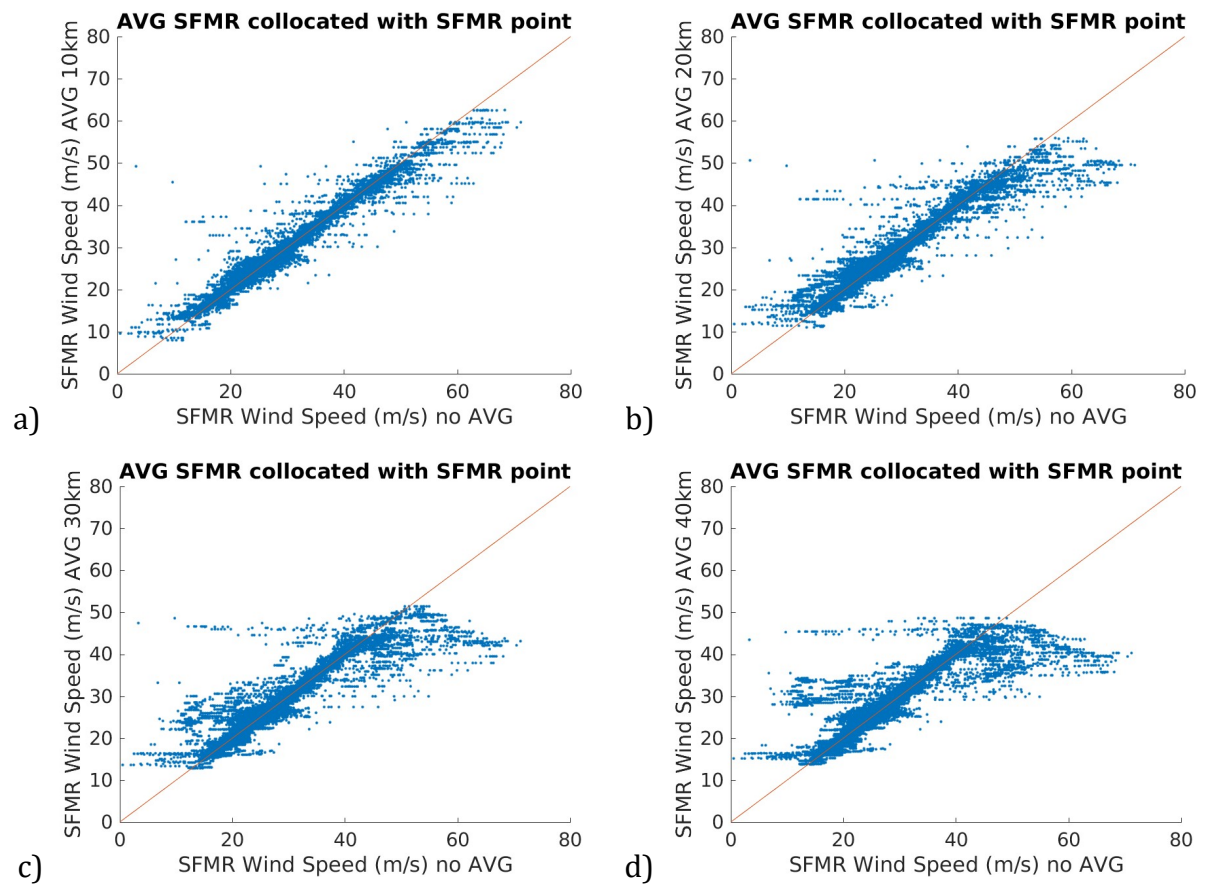


Figure 5. Scatterplot of SFMR along-track averaged versus SFMR original (non-averaged) 10-m winds. The averages are carried out over the following temporal/spatial distances: 101 sec/10 km (a), 201 sec/20 km (b), 301sec/30 km (c), 401 sec/40 km (d).

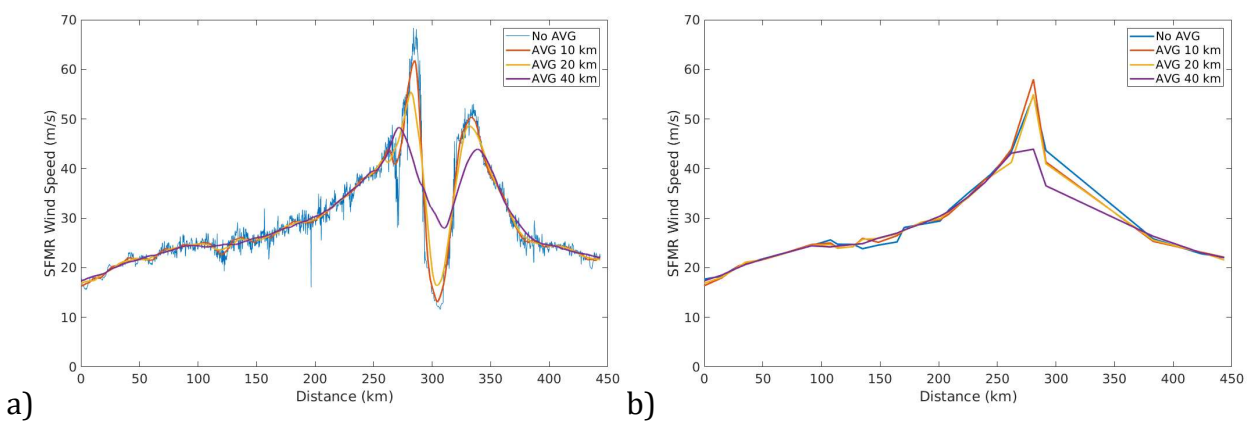


Figure 6. SFMR transect across Hurricane Matthew on October 2nd, 2016. The curves represent different SFMR along-track averaged winds (incl. non-averaged, see legend), centered at the original SFMR 1-sec sampling (a) and at the ASCAT-A sampling (b).

Figure 7 shows the same as Figure 5, but only for those SFMR points collocated with ASCAT-A, i.e., at 12.5 km subsampling. Although some SFMR averaging effects are visible, these are substantially less pronounced than in Figure 5. The reason for this is the relatively sparse sampling of the eyewall region as provided by a satellite system at 12.5 km grid spacing. Since the TC eyewall diameter typically ranges between 30 km and 60 km, a system sampling every 12.5 km will hardly ever sample the relatively narrow eyewall region, where the highest winds are found. As a result (see also Figure 6b), the collocated SFMR (non-averaged) winds (i.e., at 12.5 km subsampling) will generally not catch the storm peak winds but those of lower intensity around the eyewall region, and as such, the SFMR averaging procedure will only lead to relatively small, systematic wind differences (w.r.t. the original, non-averaged wind product).

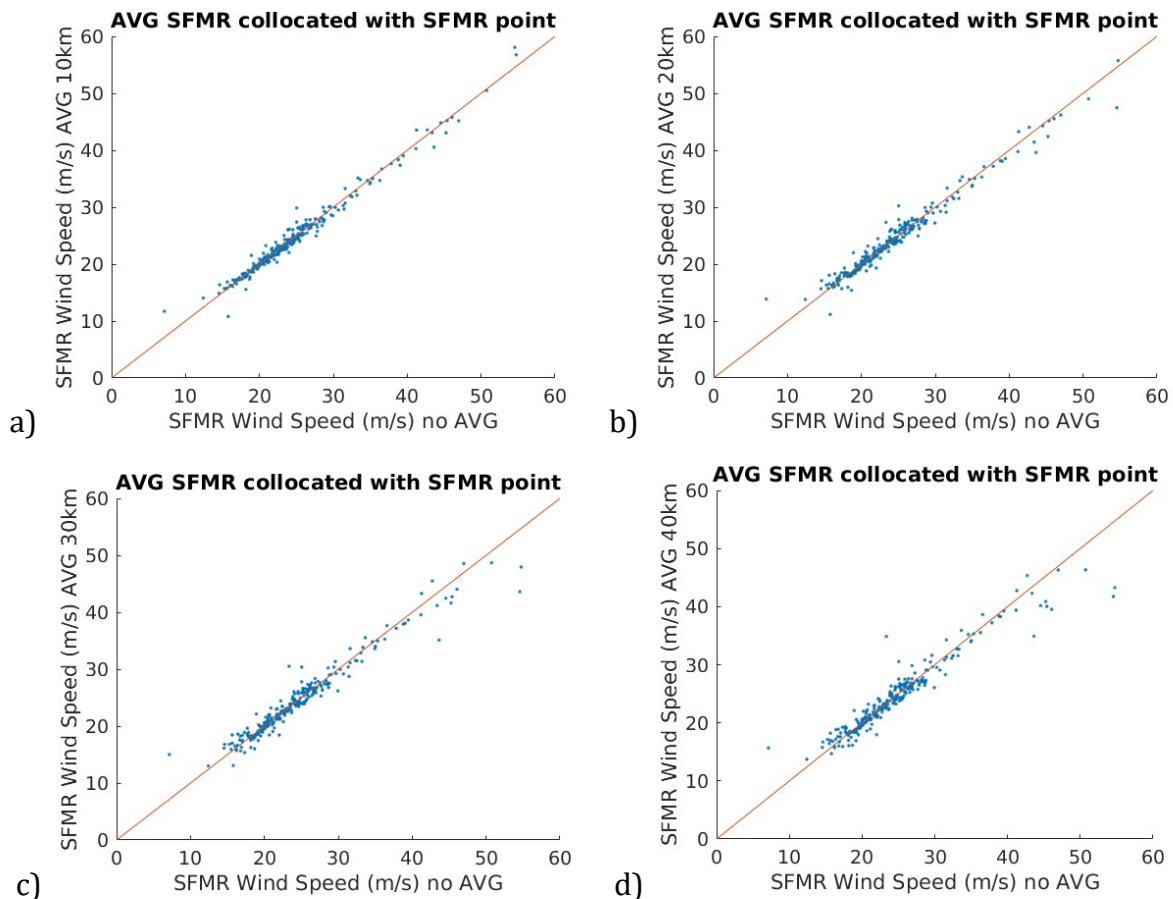


Figure 7. Same as Figure 5, but only for one Hurricane Matthew flight and for those SFMR points collocated with ASCAT-A, i.e., at 12.5 km subsampling.

Figure 8 shows a comparison between ASCAT-A 12.5 km winds and collocated SFMR winds with different along-track averagings. Taking into account that a box-car filter of width L ,

has an effective resolution of $L/\sqrt{3}$, we expect SFMR along-track averaging over 40 km to better represent ASCAT 12.5 km gridded winds, whose effective resolution is about 25 km. Indeed, ASCAT-A and SFMR winds show the least scatter for SFMR 40-km averaging. As already discussed, the impact of spatial resolution on the most extreme winds is rather small, as indicated by the reduced number of outliers in this wind regime (i.e., below the main cloud of points) in Figure 8b with respect to the other panels, notable Figure 8a.

In conclusion, the SFMR along-track averaging most representative of the satellite wind resolved scales is used in this work, i.e., 40-km (80-km) averaging for the 12.5 km (25 km) products, whose effective resolution is about 25 km (50 km). In particular, SFMR 40-km averaging is used for comparison with the ASCAT products, while SFMR 80-km averaging is used for comparison with the Ku-band scatterometers and the radiometers.

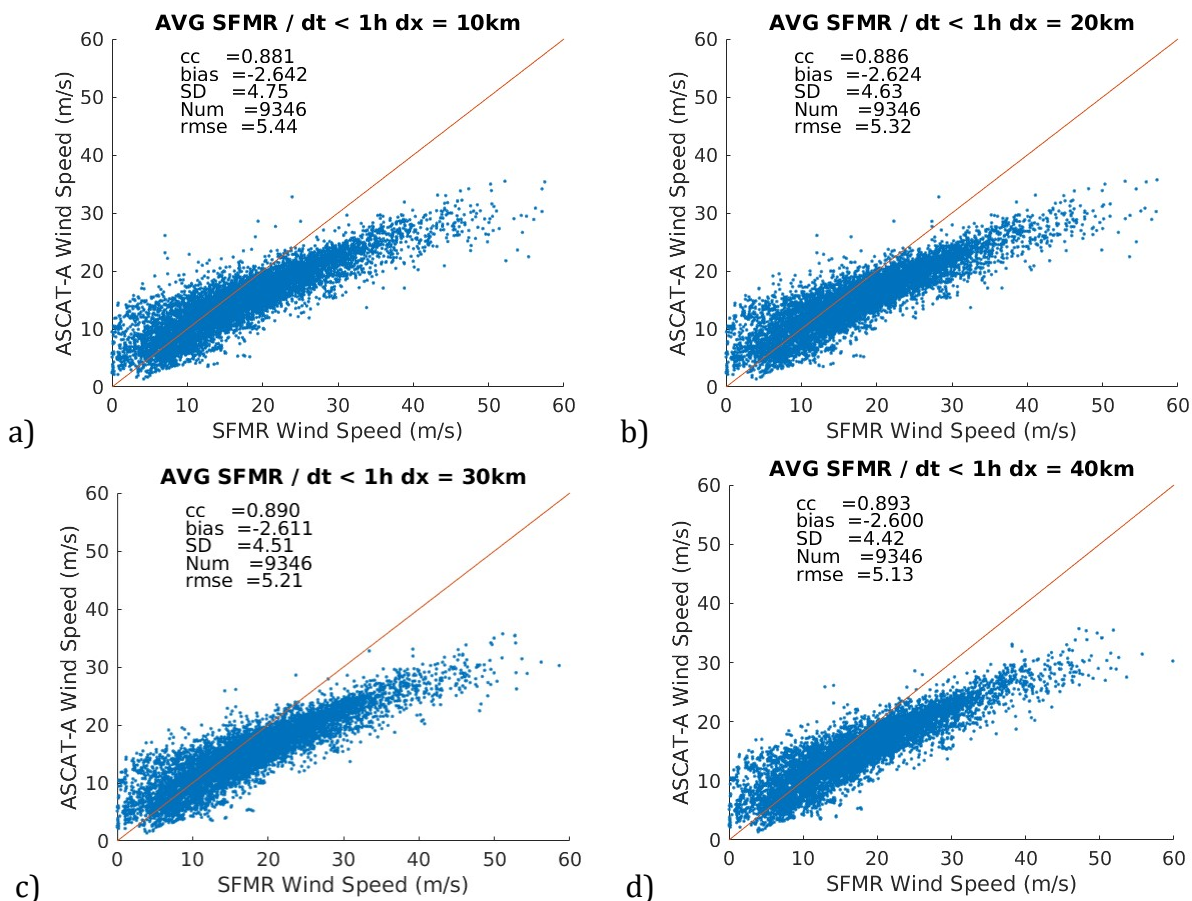


Figure 8. Scatterplot of collocated ASCAT-A winds versus SFMR along-track averaged winds over 10 km (a), 20 km (b), 30 km (c), and 40 km (d). Only collocations with $\Delta t \leq 1$ h are considered. The Pearson correlation coefficient (cc), bias, standard deviation (SD), number of points (Num), and root-mean-square error (rmse) can be found in the legend.

4 QUALITY CONTROL EFFECTS

In this section, the impact of the most relevant quality control (QC) indicators of the satellite wind products on the satellite-SFMR wind comparisons is analyzed. Based on the CHEFS project experience [Stoffelen et al., 2020], the SFMR general quality flag is ignored while SFMR winds whose retrieved rain rate is above 20 mm/h are filtered out. The SFMR-based rain rate threshold already filters out most of the poor quality SFMR winds (according to the SFMR QC flag), while keeping 96.5% of the data (not shown).

4.1 C-band scatterometer QC

Figure 9 shows the collocated ASCAT-A and SFMR winds for different ASCAT QC flags. In particular, the KNMI_QC and VAR_QC flags are tested. Note that a more general flag is also used at orbit level, the so-called product monitoring flag, i.e., when either the KNMI_QC or the VAR_QC flags are raised too often within an orbit (i.e., roughly above 8% for C-band and 20% for Ku-band systems), then all the wind data from the entire orbit are flagged. This flag is aimed at detecting instrument or ground segment anomalies and is therefore always applied in this analysis (both for C-band and Ku-band scatterometers).

The KNMI_QC is based on the GMF inversion residual, which indicates inter-beam backscatter inconsistencies due to the presence of geophysical phenomena other than the area-mean wind, such as heavy rain, high sub-WVC wind variability, or land/sea ice contamination effects [Portabella et al., 2012]. The VAR_QC instead is activated when ASCAT-derived winds are too inconsistent with the 2DVar analysis winds used in the AR scheme [Vogelzang, 2017]. Note that both the KNMI_QC and the VAR_QC accepted winds (Figures 9b and 9c, respectively) show in general a reduction of the scatter as compared to the non-filtered ASCAT-A winds (Figure 9a). However, the VAR_QC leads to the removal of most of the extreme winds. This is due to the fact that close to the eyewall, even a small misplacement of the storm centre by the 2DVar analysis (likely due to a significant misplacement of the ECMWF background winds used in the 2DVar AR scheme) leads to large inconsistencies between the ASCAT-A and the 2DVar analysis winds and therefore the activation of the VAR_QC flag. This is not necessarily an indication of poor-quality ASCAT winds. Note that the same conclusions are drawn for ASCAT-B and -C winds (not shown). Since, in this study, we are focused on the extreme wind analysis, the VAR_QC flag is disregarded, and only the KNMI_QC flag is used for filtering C-band scatterometer winds.

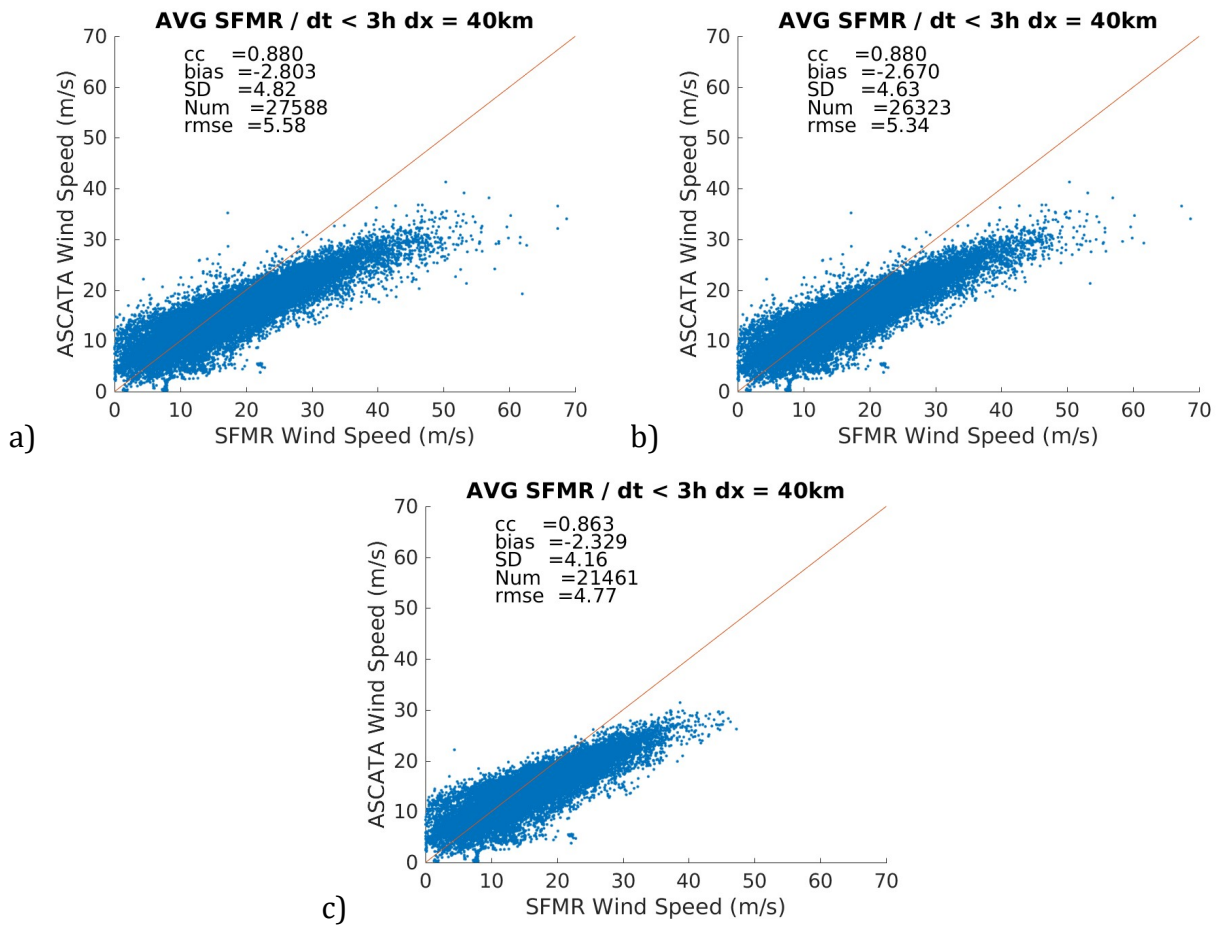


Figure 9. Scatterplot of collocated ASCAT-A versus SFMR 40-km averaged winds, for ASCAT-A no QC (a), KNMI_QC passed (b), and VAR_QC passed (c) WVCs. Only collocations with $\Delta t \leq 3$ h are considered. The same statistical parameters as in Figure 8 can be found in the legend.

4.2 Ku-band scatterometer QC

Figure 10 shows the same QC analysis as in Figure 9 but for OSCAT-2 derived winds instead of ASCAT-A. As for the ASCAT-A analysis (Figure 9), both the KNMI_QC and the VAR_QC accepted winds (Figures 10b and 10c, respectively) show in general a reduction of the scatter as compared to the non-filtered OSCAT-2 winds (Figure 10a). In contrast with the ASCAT QC, the OSCAT-2 KNMI_QC (rather than the VAR_QC) leads to the largest reduction in scatter and the removal of most of the extreme winds. While C-band scatterometer winds are found to be little impacted by rain [Lin et al., 2015], Ku-band scatterometers are substantially more perturbed by the presence of rain [Lin and Portabella, 2017], [Xu and Stoffelen, 2020]. In particular, Ku-band scatterometer winds underestimate high and extreme winds under rainy conditions [Portabella and Stoffelen, 2001]. This is clearly shown in Figure 10, since KNMI_QC

passed winds tend to less underestimate SFMR winds than unfiltered winds (see the high-wind scatter cloud being further away from the diagonal in Figure 10a than in Figure 10b). [Note that similar results are obtained for the other Ku-band scatterometer winds (not shown).] This poses a challenge for Ku-band scatterometer recalibration since one should use KNMI_QC to avoid rain contamination but on the other hand the extreme wind sampling of KNMI_QC passed WVCs is rather scarce. This issue is addressed in Section 6.

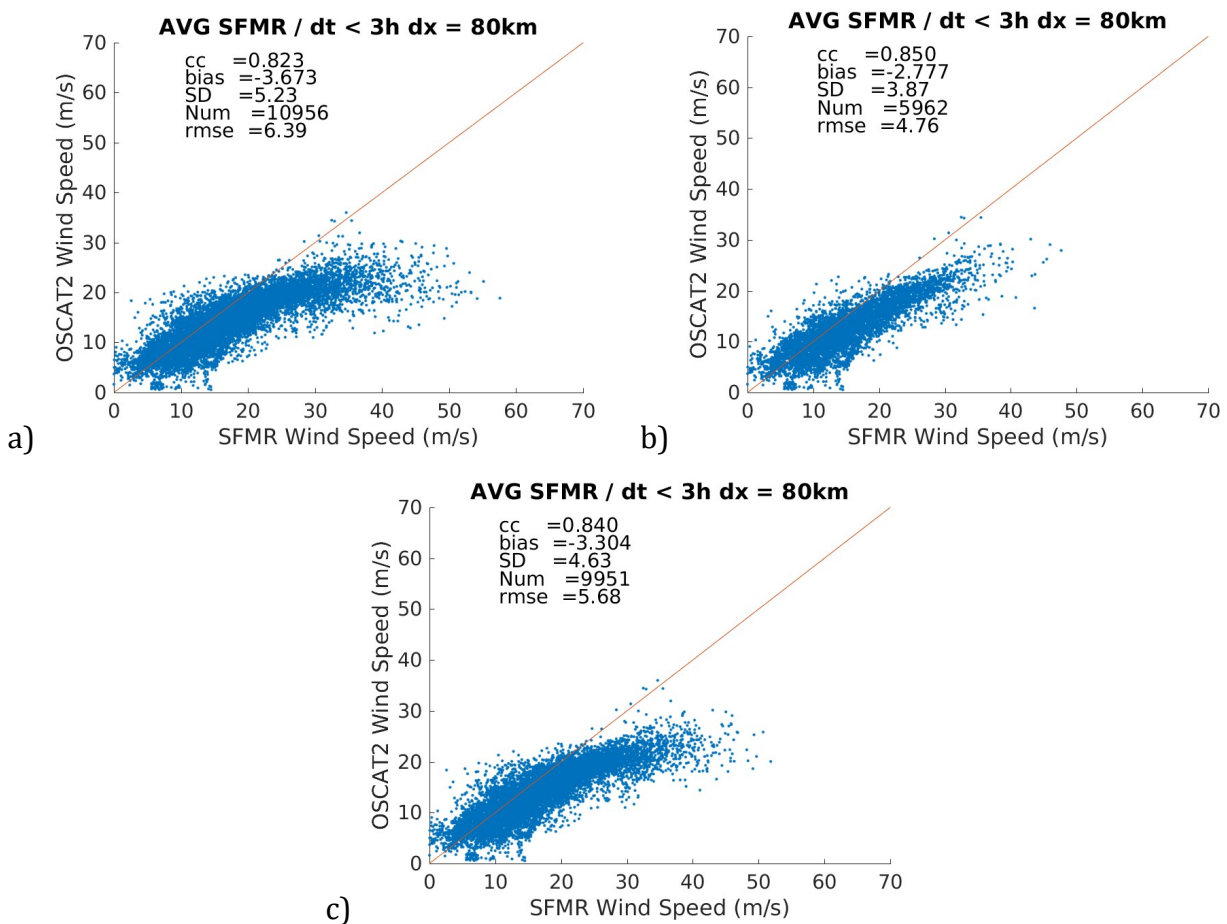


Figure 10. Scatterplot of collocated OSCAT-2 versus SFMR 80-km averaged winds, for OSCAT-2 no QC (a), KNMI_QC passed (b), and VAR_QC passed (c) WVCs. Only collocations with $\Delta t \leq 3$ h are considered. The same statistical parameters as in Figure 8 can be found in the legend.

4.3 Radiometer QC

No specific QC flags are present in the SMAP product. The SMOS product contains a QC flag indicating good, fair, and poor quality winds. While the AMSR-2 and Windsat wind products

contain a rain rate estimate which can be used for further QC purposes, poor quality winds are already set to missing values (personal communication with REMSS).

a) AMSR-2 and Windsat QC

Besides a Land/Coastal QC flag, AMSR-2 and Windsat wind products contain collocated rain rate estimates. Figure 11 shows the scatterplot of collocated AMSR-2 and SFMR winds, for AMSR-2 winds under all weather conditions (a), rain below 12 mm/h (b), and rain-free data only (c). About 5% of the data are under rainy conditions. In fact, as shown in Figure 12, the collocated dataset (with SFMR) is either under rain-free conditions (95%) or under heavy rain conditions (i.e., above 10 mm/h), according to AMSR-2 rain estimates. As shown in Figure 11, the rain estimate is not a good proxy for the data quality, since only a few outliers are removed, as indicated by the slightly decreasing SD values with rain filtering. Since Figure 11a and Figure 11b contain a few more extreme wind points than Figure 11c, which are moreover relatively close to the diagonal (i.e., showing fair agreement between AMSR-2 and SFMR winds), no strict rain-based filtering appears necessary. However, following advise from the data producer (personal communication with REMSS), AMSR-2 AW winds under rain rates below 12 mm/h are used (Figure 11b).

Similar conclusions can be drawn from the Windsat wind and rain data analysis (not shown). In conclusion, only AMSR-2 and Windsat AW winds for rain rates below 12 mm/h are used for recalibration purposes (Section 7).

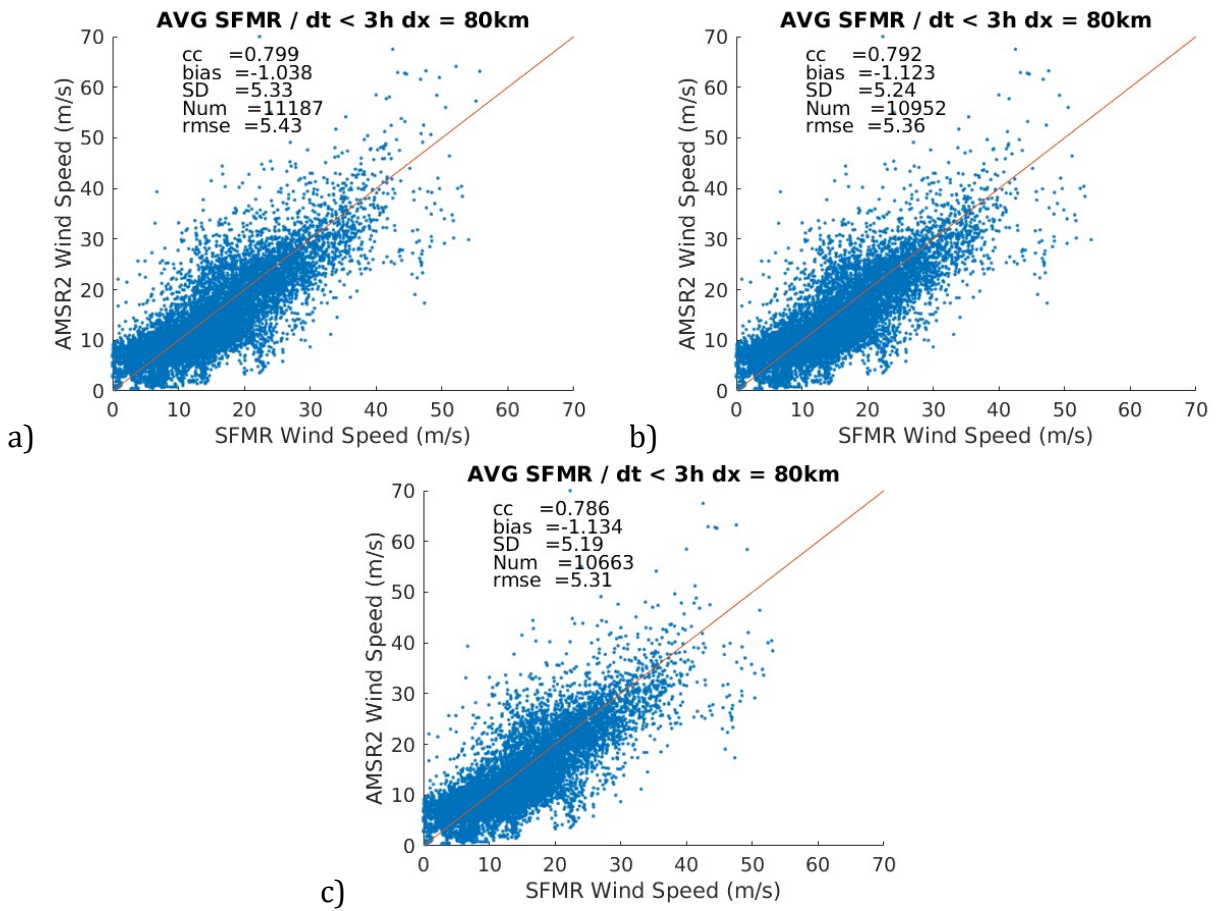


Figure 11. Scatterplot of collocated AMSR-2 versus SFMR 80-km averaged winds, for AMSR-2 all weather conditions (a), rain below 12 mm/h (b), and rain-free data only (c) WVCs. Only collocations with $\Delta t \leq 3$ h are considered. The same statistical parameters as in Figure 8 can be found in the legend.

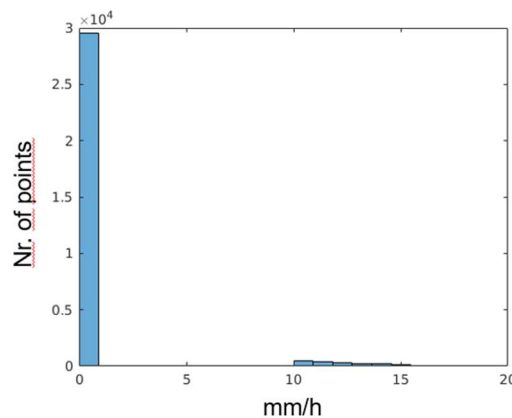


Figure 12. Histogram of AMSR-2 retrieved rain rate values, for the AMSR-2 collocated dataset shown in Figure 11.

b) SMOS QC

Figure 13 shows the scatterplots of collocated SMOS and SFMR winds, for no QC (a), SMOS good and fair quality winds only (b), and SMOS good quality winds only (c). Although the SMOS good quality winds show lower scatter (Figure 13c), these represent less than 3% of the collocated data and, in particular, very few extreme winds remain after QC. Furthermore, the SMOS good and fair quality wind dataset (Figure 13b) represents less than 30% of the collocated dataset and contains substantially less wind data above 30 m/s than the non-filtered dataset (Figure 13a), while both sets present comparable metrics (in terms of correlation, bias and SD, as shown in the legend). Therefore, to optimize extreme wind calibration, unfiltered SMOS winds are used in Section 7.

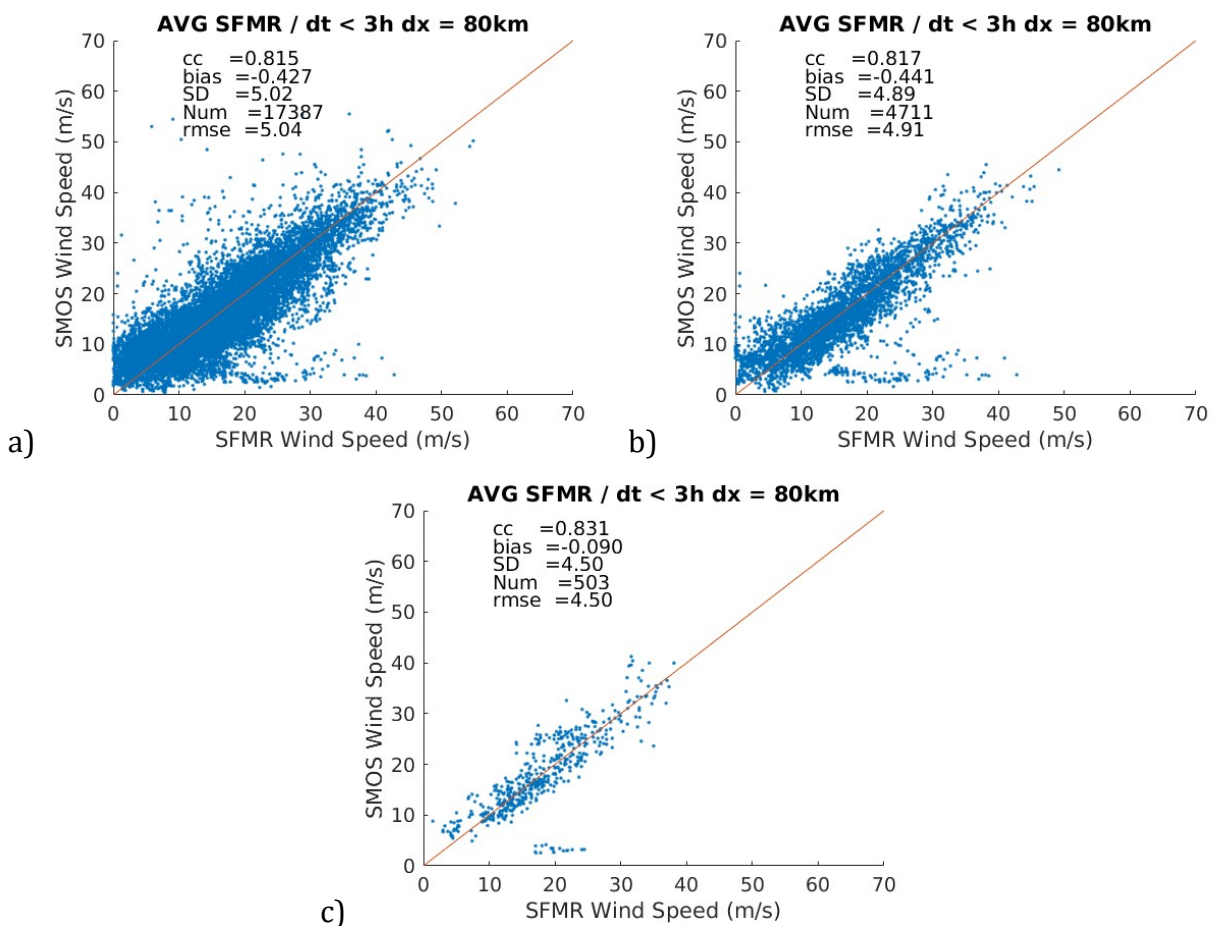


Figure 13. Scatterplot of collocated SMOS versus SFMR 80-km averaged winds, for all winds (a), only those of good or fair quality (b), and only those of good quality (c). Only collocations with $\Delta t \leq 3$ h are considered. The same statistical parameters as in Figure 8 can be found in the legend.

5 SFMR CALIBRATION EFFECTS

Each year, a SFMR in-flight ocean calibration is performed to adjust the brightness temperature (TB) calibration equation for each channel to reflect the actual conditions [Sapp et al., 2019]. The NOAA/NESDIS/STAR OSWT has inspected the provided wind data set to ensure that wind retrievals are good in terms of instrument calibration. In particular, they have excluded those winds whose corresponding TB values were not considered as reliable, because of: (i) TB differences amongst the six channels higher than 2K, suggesting the presence in the TB calibration equation of possible errors that could not be corrected; (ii) the presence of a high amount of noise in the TB channels.

To analyze potential SFMR calibration variations over time, we take the entire ASCAT-A/SFMR collocation dataset from the period 2009-2020 (see Figure 9b) and split it in six biannual datasets. To intercompare them, we take the median of each ASCAT-A versus SFMR scatterplot, computed over 45-degree rotated axes in bins of $\sqrt{2}$ m/s. The median line therefore represents the axis of symmetry for the scatterplots in, e.g., Figures 9 and 10. The resulting curves are plotted in Figure 14a. While disregarding SFMR winds below 10-15 m/s, whose quality is questionable according to [Koltz and Ulhorn, 2014], [Sapp et al., 2019], it is clear that the median curves significantly differ for SFMR winds between 15 m/s and 30 m/s. These differences can be up to 2 m/s (e.g., between the 2011-2012 and the 2019-2020 periods), i.e., large compared to the known stability of the ASCAT-A instrument, which has been reported to be within 0.1 dB (i.e., which in turn translates into 0.2 m/s for winds around 15 m/s) over a decade [Verhoef et al., 2017]. As such, they mostly correspond to SFMR calibration variations over time. This is particularly relevant in this study since we aim not only at recalibrating the satellite systems to provide winds at the SFMR wind scale, but also at producing well inter-calibrated satellite wind datasets.

Figure 14b shows similar median curves to those in Figure 14a, but for the time periods of the other scatterometer and radiometer data records. Again, a similar variation between curves can be seen, compared to that of Figure 14a. For example, differences up to 2 m/s can be seen in the range 15-30 m/s between the OSCAT (red) or HSCAT-A (black) periods and the ASCAT-C or HSCAT-B (purple) periods. This indicates that by using SFMR as recalibration reference for each scatterometer, a poor inter-calibration of the different scatterometers will be achieved. The same conclusions can be drawn for the SFMR-based recalibration of the radiometer systems. This issue is addressed in Sections 6 and 7.

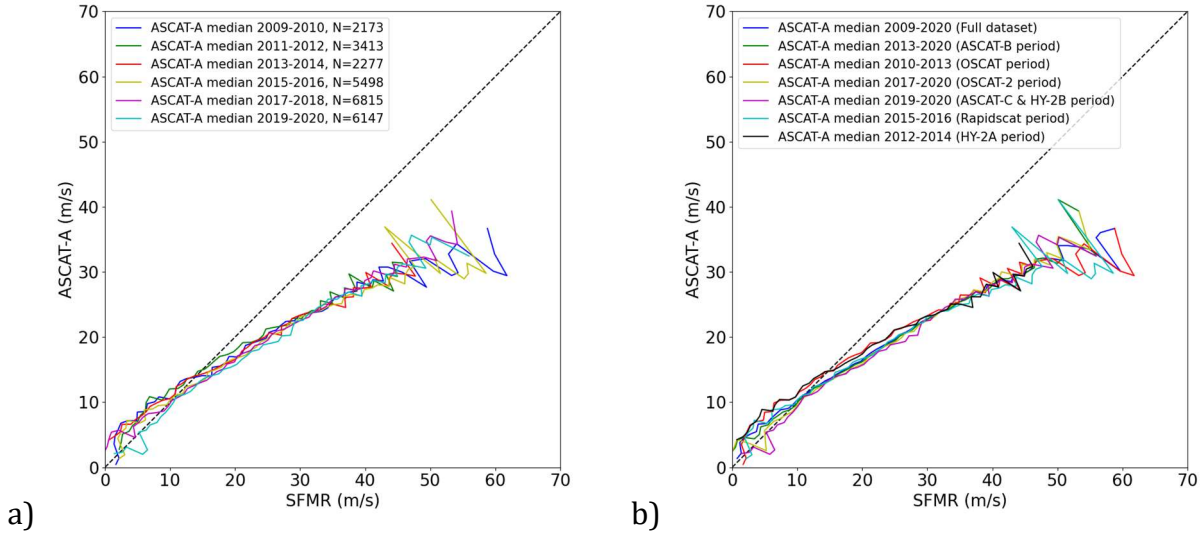


Figure 14. Median curves of the scatterplots of collocated ASCAT-A KNMI_QC passed versus SFMR 40-km averaged winds for six consecutive biannual periods (a) and for other scatterometer coincident periods (b) (see coloured legend). Only collocations with $\Delta t \leq 3$ h are considered.

6 SCATTEROMETER RECALIBRATION

Following the collocation methodology (Section 2) and accounting for the spatial resolution (Section 3) and QC (Section 4) effects, we perform an SFMR-based recalibration of the mentioned scattermeters (in this Section) and radiometers (in Section 7). Moreover, because of the SFMR calibration mentioned effects (Section 5) and the need for inter-calibrated datasets, satellite-satellite collocations are used to fine tune the recalibration functions using ASCAT recalibrated winds as reference.

6.1 C-band systems

Figure 15 shows the contourplots of collocated ASCAT-A (a), ASCAT-B (b), and ASCAT-C (c) KNMI_QC passed WVCs versus SFMR 40-km averaged winds for the periods 01/2009-12/2020, 11/2012-12/2020, and 01/2019-12/2020, respectively. As expected from the relatively small SFMR calibration variations seen in Figure 14b between the ASCAT-A (dark blue), ASCAT-B (dark green), and ASCAT-C (purple) time periods, the three contourplots in

Figure 15, which represent the different time periods, only show small differences at high winds (i.e., between 15 and 30 m/s). In particular, ASCAT-C winds (Figure 15c) are slightly lower than ASCAT-A (Figure 15a) and ASCAT-B (Figure 15b) winds in the mentioned wind regime, in line with Figure 14b.

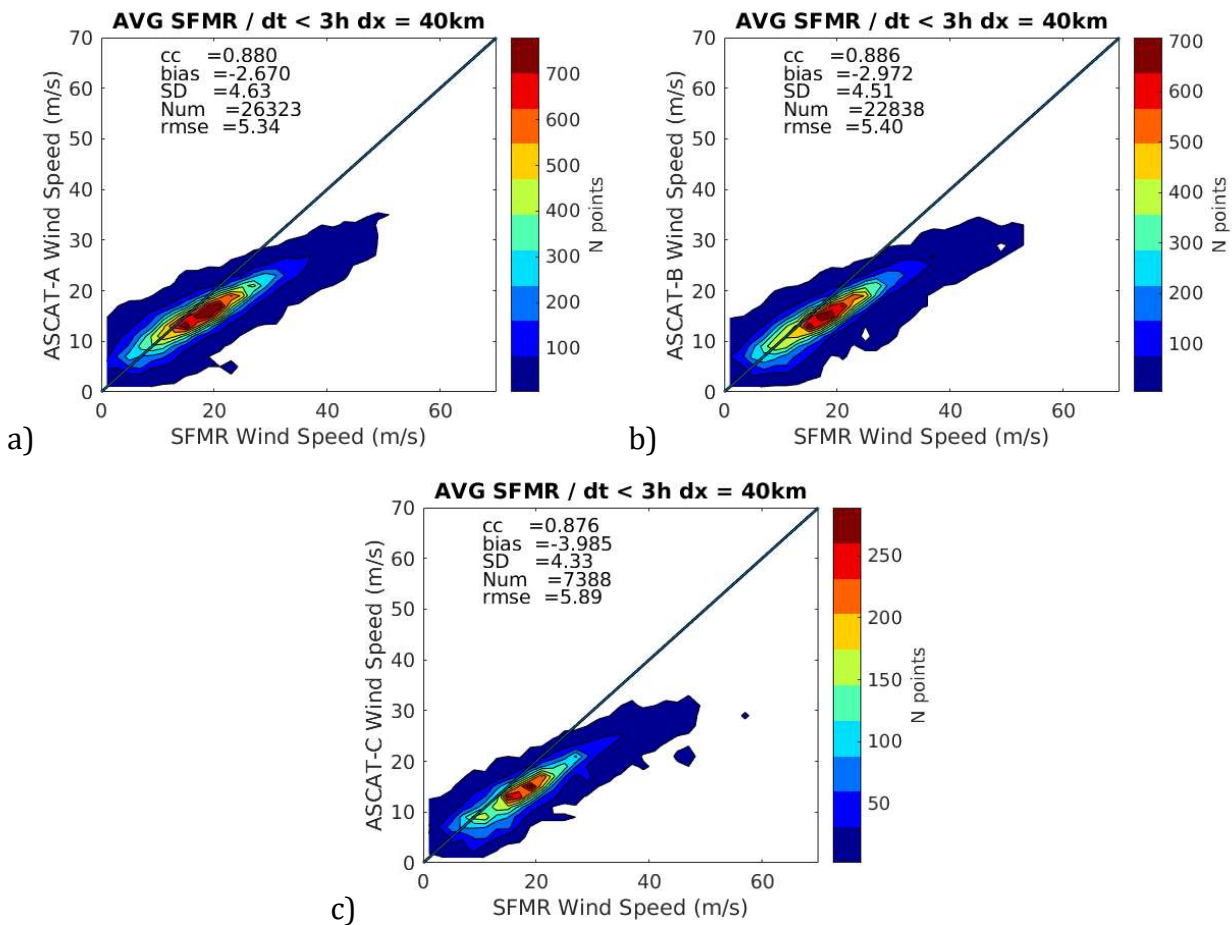


Figure 15. Contourplot of collocated ASCAT-A (a), ASCAT-B (b), and ASCAT-C (c) KNMI_QC passed WVCs versus SFMR 40-km averaged winds, for the periods 01/2009-12/2020, 11/2012-12/2020, and 01/2019-12/2020, respectively. Only collocations with $\Delta t \leq 3$ h are considered. The same statistical parameters as in Figure 8 can be found in the legend.

Figure 16 shows the same contourplots of collocated ASCAT-A (a), ASCAT-B (b), and ASCAT-C (c) KNMI_QC passed WVCs versus SFMR 40-km averaged winds from Figure 15, but for the same period, i.e., 2019. Again, the three systems show a similar behavior with respect to SFMR averaged winds. On the one hand, the three ASCAT wind sources are generated with the same processor (AWDP). On the other hand, while SFMR calibration changes are observed from

year to year (see Section 5), we expect smaller calibration effects when analyzing a single year. The differences between the three ASCATs can actually be associated to differences in the weather sampling. As such, we conclude that for recalibration purposes, it is relevant to maximize high and extreme wind sampling.

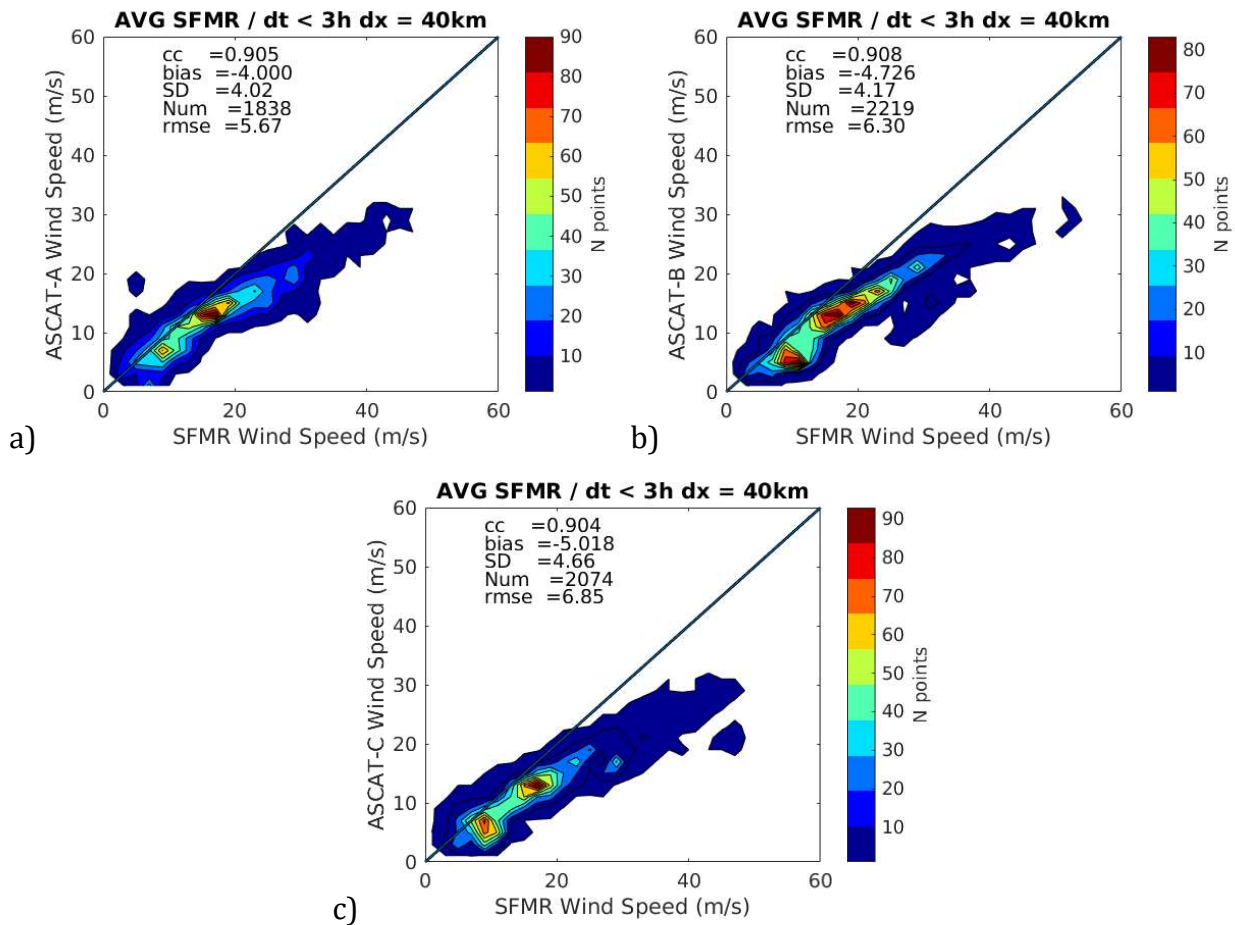


Figure 16. Contourplot of collocated ASCAT-A (a), ASCAT-B (b), and ASCAT-C (c) KNMI_QC passed WVCs versus SFMR 40-km averaged winds, for the year 2019. Only collocations with $\Delta t \leq 3$ h are considered. The same statistical parameters as in Figure 8 can be found in the legend.

Recalibration strategy

The SFMR calibration temporal changes reported in Section 5 pose a real challenge on satellite-derived extreme wind recalibration efforts. Not so much for recalibrating the three ASCATs (as discussed above), but for recalibrating all scatterometer and radiometer systems while ensuring good inter-calibration between them. Since we have no indication on which

SFMR calibration (see Figure 14) is the most accurate one, we assume a mean SFMR calibration over the period of interest, i.e., 2009-2020.

Figure 17 shows the scatterplot of collocated ASCAT WVCs versus SFMR 40-km averaged winds, for the period 2009-2020. This includes ASCAT-A, -B, and -C for the periods 01/2009-12/2020, 11/2012-12/2020, and 01/2019-12/2020, respectively. Note that the goal is to recalibrate satellite-derived high and extreme winds. Moreover, since SFMR low wind quality is questionable [Koltz and Ulhorn, 2014], [Sapp et al., 2019], only winds above 10-15 m/s are considered.

The median of the scatterplot (red curve), computed over 45-degree rotated axes, is taken as reference for fitting a second-order polynomial function (purple curve) for winds above 12 m/s. The expression for the latter is:

$$U_{10s}^* = 0.01847U_{10s}^2 + 1.035U_{10s} - 2.985; \forall U_{10s} > 11.8 \text{ m/s} \quad (2)$$

Where U_{10s} and U_{10s}^* represent the ASCAT original and recalibrated wind speed, respectively. Note that there is a slight misfit between the median curve and the recalibration function around 12-15 m/s. The recalibration function has a smoother departure from the diagonal. This is done to avoid sharp changes in the ASCAT recalibrated winds, which can cause artifacts, e.g., in the wind derivatives.

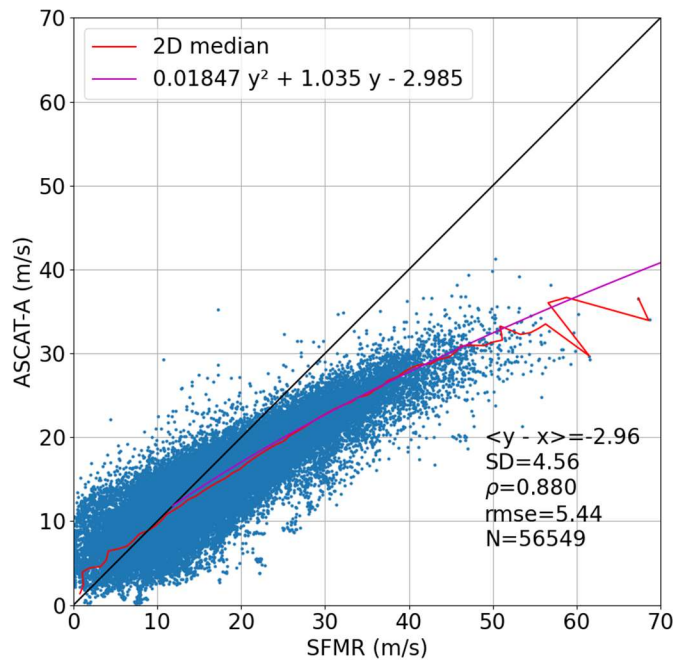


Figure 17. Scatterplot of collocated ASCAT-A/-B/-C KNMI_QC passed WVCs versus SFMR 40-km averaged winds, for the period 2009-2020, together with the median curve (dark blue) and the polynomial function fit (Eq. 2, light blue) derived from the scatterplot. Only collocations with $\Delta t \leq 3$ h are considered. The same statistical parameters as in Figure 8 can be found in the legend.

Figure 18 shows the contourplot of ASCAT-A/-B/-C winds versus SFMR averaged winds, before (a) and after (b) recalibration. As shown in Figure 18b, the ASCAT recalibrated winds are in good agreement with those of SFMR, indicating the effectiveness of the recalibration function (Eq. 2).

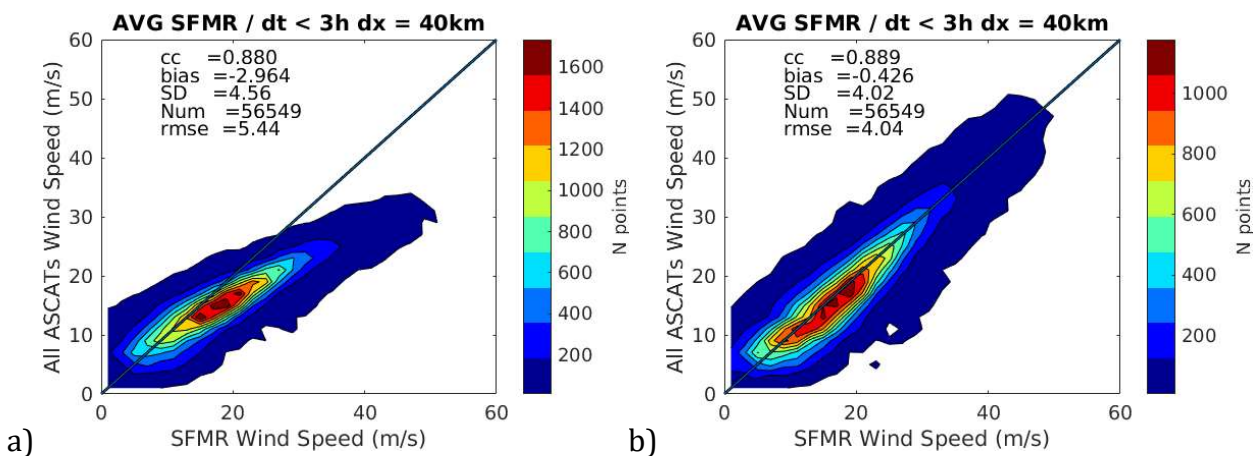


Figure 18. Contourplots of collocated ASCAT-A/-B/-C KNMI_QC passed WVCs versus SFMR 40-km averaged winds, for the period 2009-2020 and for the original (a) and recalibrated (b) ASCAT winds. Only collocations with $\Delta t \leq 3$ h are considered. The recalibration function is shown in Eq. 2. The same statistical parameters as in Figure 8 can be found in the legend.

6.2 Ku-band systems

A similar recalibration strategy to that of the C-band systems (see Section 6.1) is undertaken in this section. As for the C-band ASCATs, each Ku-band scatterometer operates on a different period: 01/2010-02/2014 (OSCAT), 06/2012-04/2015 (HSCAT-A), 11/2014-08/2016 (RapidScat), 01/2017-12/2020 (OSCAT-2), 01/2019-12/2020 (HSCAT-B). Since all the Ku-band scatterometers are processed with the same processor (PenWP), they are expected to be fairly inter-calibrated. As such, SFMR calibration variations over time are expected to dominate over residual Ku-band scatterometer inter-calibration issues. Similar to the ASCATs recalibration, the Ku-band recalibration is performed over the joined Ku-band scatterometer datasets collocated with SFMR winds.

Figure 19 shows the scatterplot of collocated Ku-band scatterometer (i.e., OSCAT, HSCAT-A, RapidScat, OSCAT-2, HSCAT-B) VAR_QC passed WVCs versus SFMR 80-km averaged winds for the period 01/2010-12/2020. Note that the KNMI_QC flagged WVCs (which include rain-contaminated cases) are shown in yellow. It is clear that most of the extreme wind points are

KNMI_QC flagged, indicating rain-contamination effects near the hurricane eyewall region. By fitting a polynomial function over all the points, the shape of the function at the extreme wind regime is clearly dominated by rain contaminated winds. This function is expressed as:

$$U_{10s}^* = 0.05659U_{10s}^2 - 0.1145U_{10s} + 5.272; \forall U_{10} > 11.8 \text{ m/s} \quad (3)$$

Where U_{10s} and U_{10s}^* represent the Ku-band original and recalibrated scatterometer wind speed, respectively.

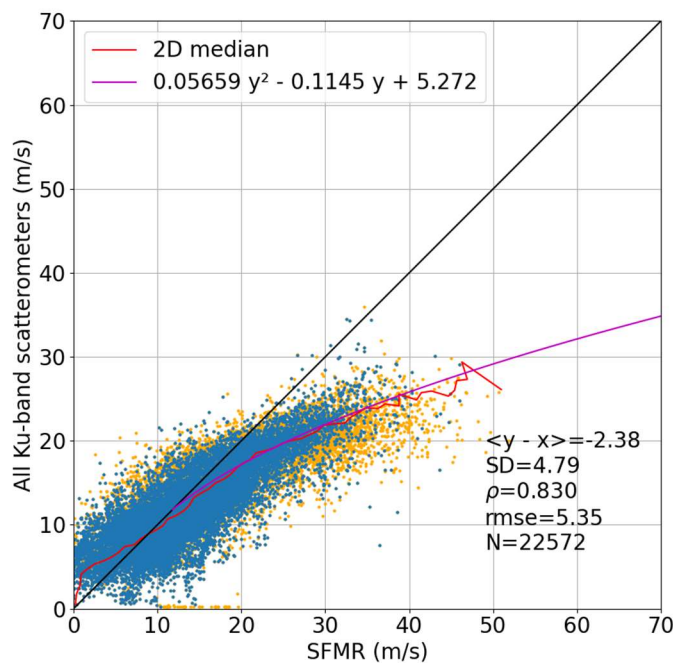


Figure 19. Scatterplot of collocated Ku-band scatterometer (i.e., OSCAT, HSCAT-A, RapidScat, OSCAT-2, HSCAT-b) VAR_QC passed WVCs versus SFMR 80-km averaged winds, for the period 2009-2020, together with the median curve (red) and the polynomial function fit (Eq. 3, purple) superimposed. Note that KNMI_QC flagged winds are marked as yellow dots. Only collocations with $\Delta t \leq 3$ h are considered. The same statistical parameters as in Figure 8 can be found in the legend.

Figure 20 shows the contourplot of Ku-band scatterometer winds versus SFMR averaged winds, before (a) and after (b) recalibration. As shown in Figure 20b, the recalibrated Ku-band scatterometer winds are in good agreement with those of SFMR, indicating the effectiveness of the recalibration function (see statistical parameters in the legend). Note a slight underestimation of Ku-band scatterometer winds in the range 10-15 m/s. This is due to a slight misfit between the median curve and the recalibration function (see Figure 19). As for

the C-band recalibration function, the Ku-band function has a smoother departure from the diagonal than the median curve to avoid artifacts in the, e.g., wind derivatives.

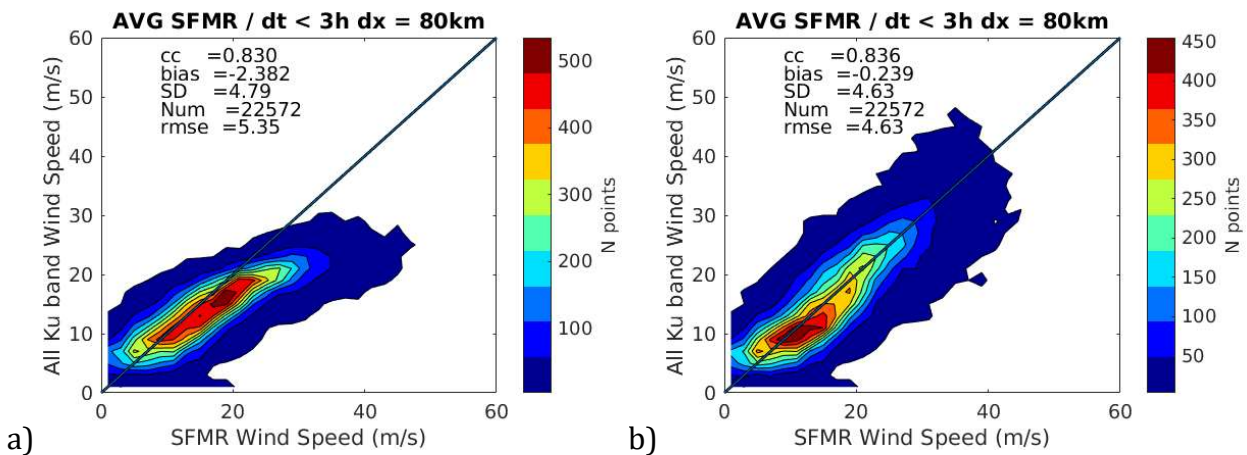


Figure 20. Contourplots of collocated Ku-band scatterometer (i.e., OSCAT, HSCAT-A, RapidScat, OSCAT-2, HSCAT-B) VAR_QC passed WVCs versus SFMR 80-km averaged winds and for the original (a) and recalibrated (b) Ku-band scatterometer winds. Only collocations with $\Delta t \leq 3$ h are considered. The recalibration function is shown in Eq. 3. The same statistical parameters as in Figure 8 can be found in the legend.

However, when collocating OSCAT-2 winds with ASCAT-A winds, a clear mismatch is found for winds above 15 m/s. Figure 21 shows the contourplots of OSCAT-2 versus collocated ASCAT-A original (a) and recalibrated (b) winds, for a period of one year (2017), with the following spatial and temporal distance criteria: the closest within 25 km and 30 minutes. Note though that most of the collocations are within 15 minutes since OSCAT-2 and ASCAT-A orbits were quite similar in 2017. It is clear that while the original datasets are in good agreement, an S-shape is found in the contourplot of the recalibrated datasets (Figure 19b), indicating underestimation (overestimation) of OSCAT-2 winds with respect to ASCAT-A winds, between 15 and 20 m/s (above 20 m/s). This indeed shows that recalibrating Ku-band winds by neglecting the KNMI_QC flag leads to poorly inter-calibrated C- and Ku-band scatterometers.

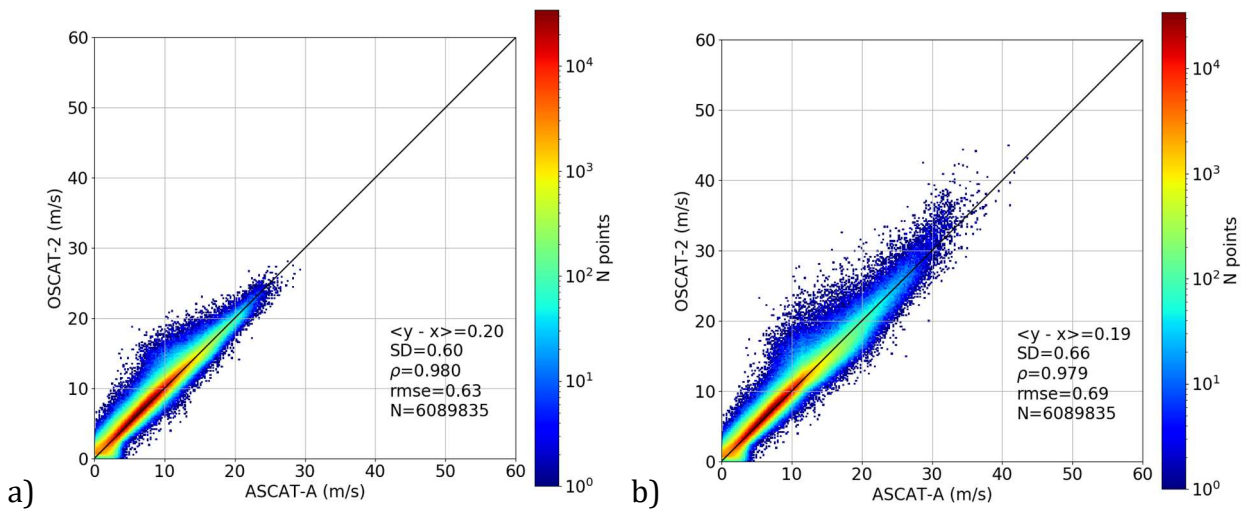


Figure 21. Contourplots of OSCAT-2 versus ASCAT-A collocated winds, for the original (a) and recalibrated (b) datasets, and the year 2017. Note that the recalibration is performed by applying Eqs. 2 and 3 to the ASCAT-A and OSCAT-2 winds, respectively. The same statistical parameters as in Figure 8 can be found in the legend.

However, if Ku-band scatterometer KNMI_QC passed winds are used for recalibration in Figure 19 (i.e., only the blue points), very few extreme wind samples are kept, not enough to fit an extreme wind recalibration function. Note also that, as seen in Figure 21a, OSCAT-2 and ASCAT-A winds show in general very good correlation and inter-calibration, suggesting that the C-band recalibration function (Eq. 2) can actually be applied to recalibrate the Ku-band systems and in turn ensure good C-/Ku-band scatterometer inter-calibration, also at extremes (for non rain contaminated Ku-band winds).

Figures 22 and 23 show the same contourplot as in Figure 21b, but for each Ku-band scatterometer separately, recalibrated with either Eq. 3 (left) or Eq. 2 (right). [Figure 21b is identical to Figure 22a for convenience.] Note that the scatter is quite different for different Ku-band scatterometers. The main reason for this is the different temporal distance used in the collocations, which directly depends on the orbit characteristics of each system with respect to that of ASCAT-A. For those Ku-band systems with orbits not matching those of ASCAT-A, a longer temporal window is selected to allow more collocations, which will in turn increase the collocation errors, leading to a larger scatter in the scatterplots. The following temporal distances have been used: 30 minutes (OSCAT-2), 3 hours (OSCAT), 15 minutes (Rapidscat), 3 hours (HSCAT-A and -B).

It is clear that the C-band recalibration function (Eq. 2) leads to better inter-calibration of C- and Ku-band datasets and, as such, the latter is used for recalibration of all scatterometer datasets. This will in turn produce Ku-band extreme wind underestimation near the hurricane eyewall, which is expected due to rain contamination of the Ku-band signal.

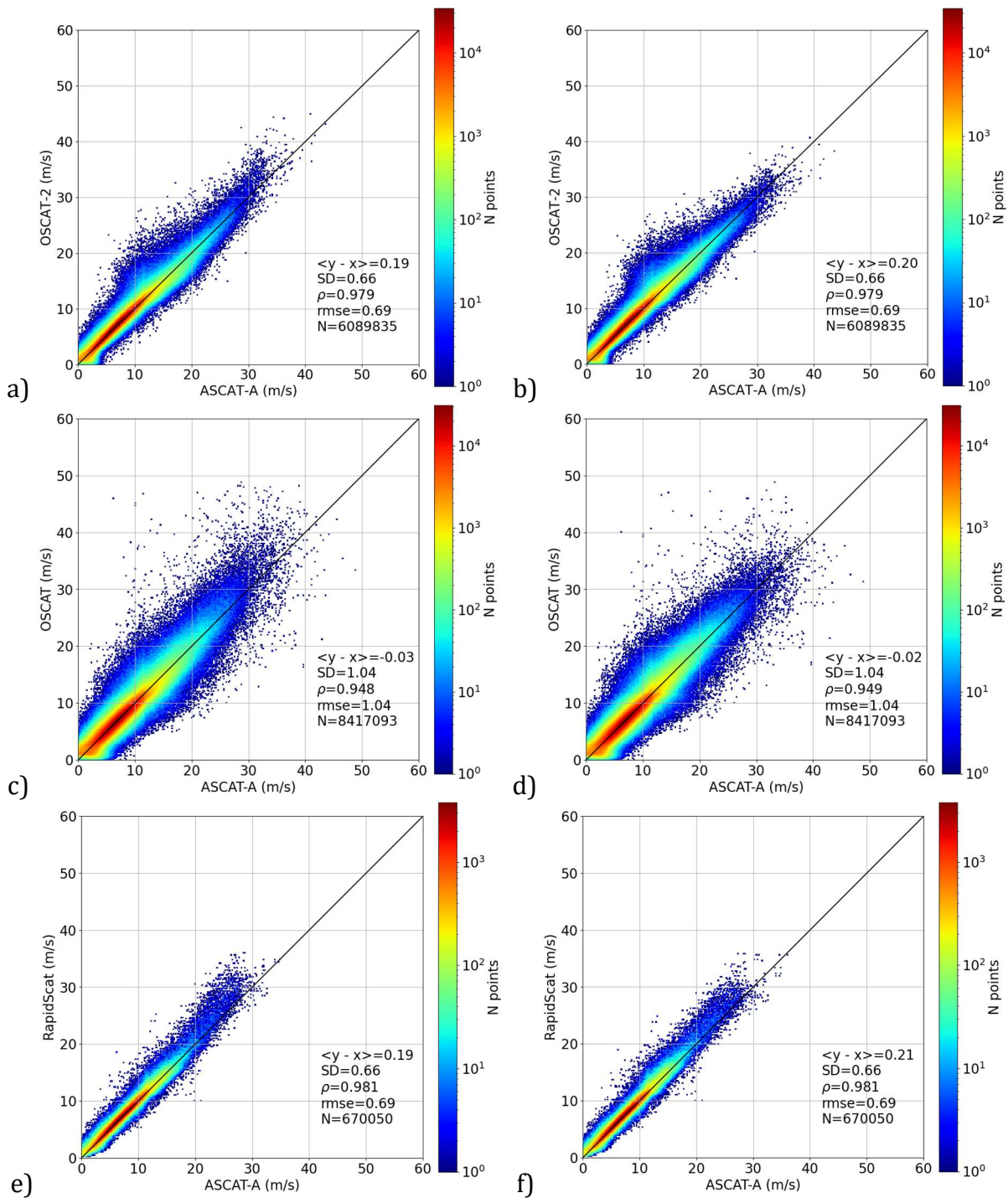


Figure 22. Contourplots of OSCAT-2 (top), OSCAT (middle), and RapidScat (bottom) recalibrated winds versus collocated ASCAT-A recalibrated winds, for the periods 01/2017-12/2017, 01/2013-12/2013, and 01/2015-12/2015, respectively. The Ku-band scatterometer recalibration is computed with the Ku-band function (Eq. 3, left) and the C-band function (Eq. 2, right). The same statistical parameters as in Figure 8 can be found in the legend.

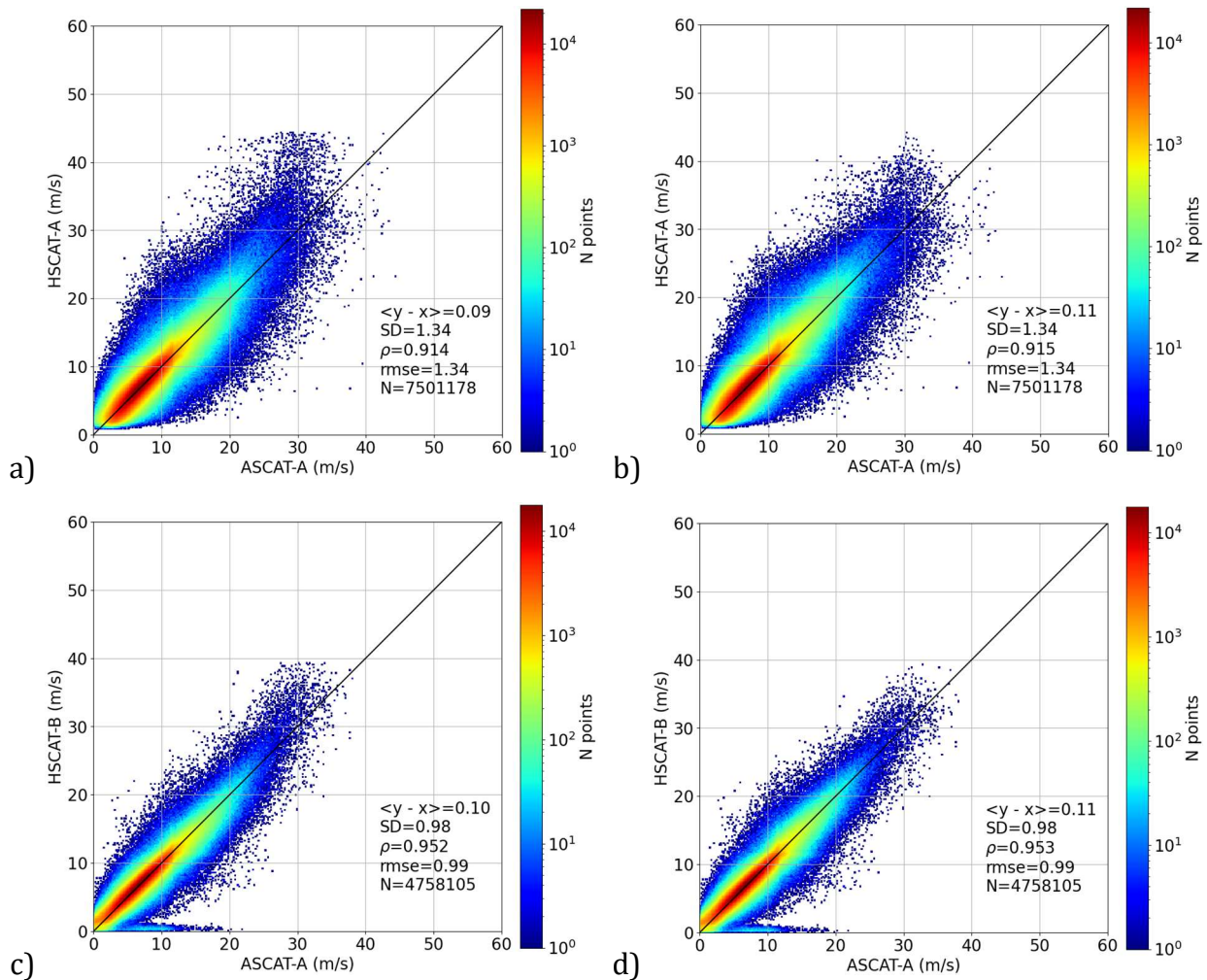


Figure 23. Contourplots of HSCAT-A (top) and HSCAT-B (bottom) recalibrated winds versus collocated ASCAT-A recalibrated winds, for the periods 01/2013-12/2013 and 01/2020-12/2020, respectively. The Ku-band scatterometer recalibration is computed with the Ku-band function (Eq. 3, left) and the C-band function (Eq. 2, right). The same statistical parameters as in Figure 8 can be found in the legend.

7 RADIOMETER RECALIBRATION

Following the strategy for recalibrating C-band and Ku-band scatterometers, we aim at recalibrating extreme winds using SFMR winds as reference while ensuring proper intercalibration with C-band and Ku-band winds in the moderate and high wind regimes. As such,

ASCAT recalibrated winds will also be used to further tune the radiometer recalibration function. In doing so, we also account for SFMR calibration variations (see Sections 5 and 6.1).

7.1 AMSR-2

Figure 24 shows AMSR-2 winds (for rain rates below 12 mm/h) versus collocated SFMR 80-km averaged winds (a) and ASCAT-A winds (b). While the entire AMSR-2 data record (07/2012-12/2020) is used in Figure 24a, a shorter period of 6 months is used in Figure 24b (05/2016-10/2016) since a large number of direct AMSR-2/ASCAT collocations is available, provided that a temporal window of 3 hours is allowed (due to the different orbit local Equator crossing times of both systems).

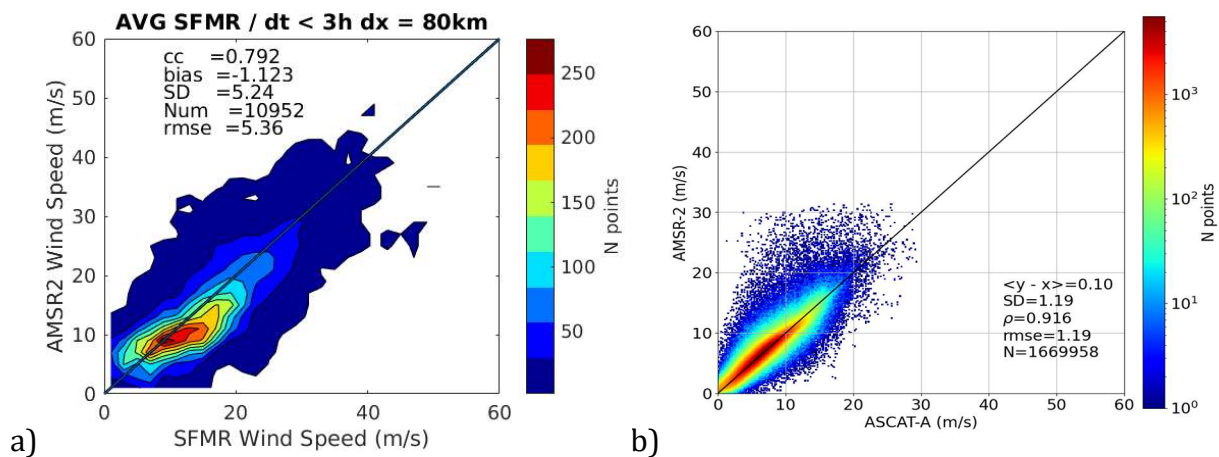


Figure 24. Contourplots of AMSR-2 winds (only wind data for rain below 12 mm/h) versus collocated SFMR 80-km averaged winds (a) and ASCAT-A winds (b). Only collocations with $\Delta t \leq 3$ h are considered. The same statistical parameters as in Figure 8 can be found in the legend.

At the extreme wind regime (i.e., SFMR winds above 30 m/s), while AMSR-2 winds are significantly noisier than scatterometer winds (see the relatively large scatter in Figure 24a as compared to that of Figures 18a and 20a), the former show no significant bias with respect to SFMR winds, indicating a fair calibration under extreme wind conditions. However, note the AMSR-2 anomalous behavior for SFMR winds in the range 10-20 m/s (Figure 24a), which is not observed with scatterometer winds (Figures 18a and 20a). Moreover, when collocating ASCAT and AMSR-2 winds (Figure 24b), both datasets show fairly good inter-calibration in the range 10-20 m/s. Since the vast majority of the ASCAT/AMSR-2 direct collocations are acquired away from TCs, it is concluded that the AMSR-2 moderate and high wind retrievals

are of poor quality under TC conditions. Note that the same anomalous behavior appears when repeating Figure 24a for rain-free conditions (not shown). This issue needs further investigation and has already been reported to REMSS.

To ensure good inter-calibration between the ASCAT recalibrated winds (Section 6.1) and the AMSR-2 winds, a recalibration of AMSR-2 moderate and high winds is proposed in Figure 25. Since AMSR-2 extreme winds are already aligned with SFMR winds (see Figure 24a), the polynomial fit in Figure 25 is only applied for winds in the range 10-38 m/s. The fit consists of the following 3rd order polynomial function:

$$U_{10s}^* = -0.0002353U_{10}^3 + 0.005741U_{10s}^2 + 1.165U_{10} - 1.842; \forall U_{10s} \in [10, 38] \text{ m/s} \quad (4)$$

Where U_{10s} and U_{10s}^* represent the AMSR-2 original and recalibrated wind speed, respectively.

Figure 25b shows indeed good inter-calibration between AMSR-2 recalibrated winds (using Eq. 4) and ASCAT-A recalibrated winds (using Eq. 2). Figure 26 shows the AMSR-2 recalibrated winds against collocated SFMR winds. In comparison with AMSR-2 original winds (Figure 24a), the AMSR-2 recalibrated winds show a slightly better alignment with SFMR winds in the range 20-30 m/s (Figure 26). Note that by construction both the original (Figure 24a) and the recalibrated (Figure 26) extreme winds show good alignment with SFMR winds. However, the already mentioned anomalous behavior of AMSR-2 original winds (for SFMR winds in the range 10-20 m/s) remains after recalibration. Again, this anomalous behavior, which is only found under TC conditions, needs further investigation.

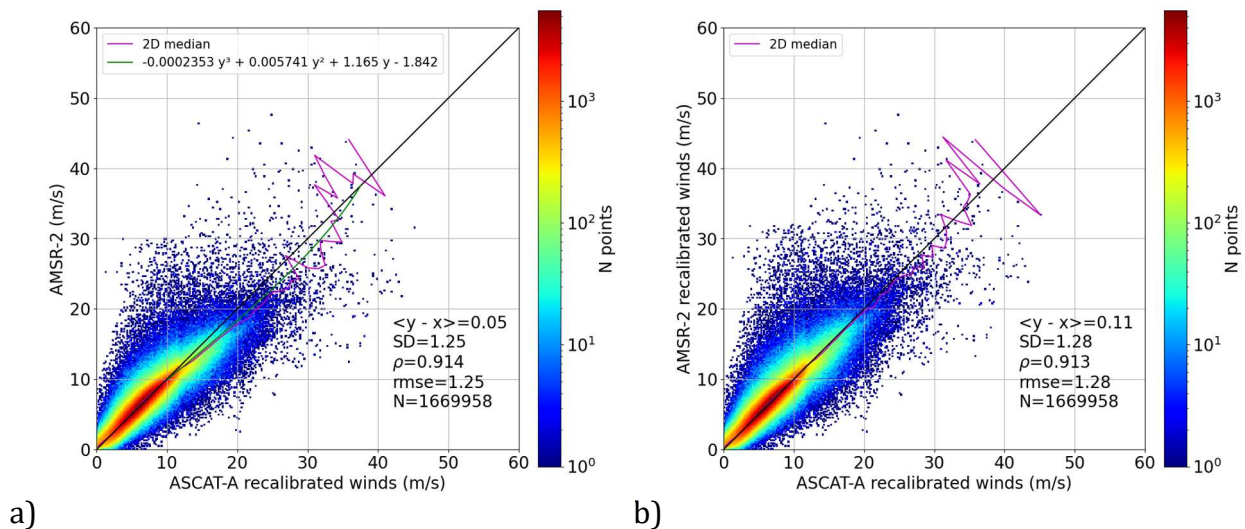


Figure 25. (a) Contourplot of AMSR-2 winds (only wind data for rain below 12 mm/h) versus ASCAT-A recalibrated winds, together with the median curve (purple) and the polynomial function fit (green) superimposed; (b) contourplot of Windsat recalibrated winds versus ASCAT-A recalibrated winds, together with the median curve (purple). Only collocations with $\Delta t \leq 3$ h are considered. The AMSR-2 recalibration function is shown in Eq. 4. The same statistical parameters as in Figure 8 can be found in the legend.

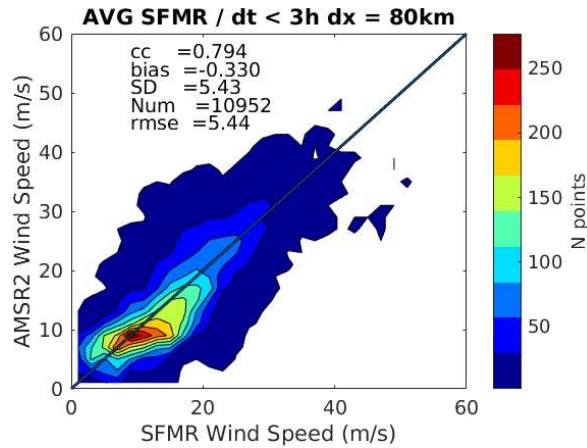


Figure 26. Contourplot of AMSR-2 recalibrated winds versus collocated SFMR 80-km averaged winds. Only collocations with $\Delta t \leq 3$ h are considered. The AMSR-2 recalibration function is shown in Eq. 4. The same statistical parameters as in Figure 8 can be found in the legend.

7.2 Windsat

Figure 27 shows Windsat winds (for rain rates below 12 mm/h) versus collocated SFMR 80-km averaged winds (a) and ASCAT-A winds (b). While the entire Windsat data record since 2010 is used in Figure 27a (01/2010-10/2020), a shorter period of of 6 months is used in Figure 27b (05/2016-10/2016).

Windsat AW winds show a similar anomalous wind pattern for SFMR winds in the range 10-20 m/s (Figure 27a) to that found for AMSR-2 AW winds (Figure 24a), which is not present when comparing Windsat and ASCAT-A winds (Figure 27b), further confirming that, under TC conditions, higher frequency radiometer derived moderate and high winds are of questionable quality. In contrast with AMSR-2 AW winds, Windsat AW winds show a clear misalignment with SFMR winds at the high and extreme wind regimes. As already mentioned in Section 2.1, a new Windsat AW version 8 wind product is currently under development, which aims at improved high and extreme wind retrievals, similar to what REMSS has done for the AMSR-2 AW version 8.2 [Meissner et al., 2021]. For the time being, we focus our efforts on recalibrating the currently available Windsat AW version 7.0.1 wind product.

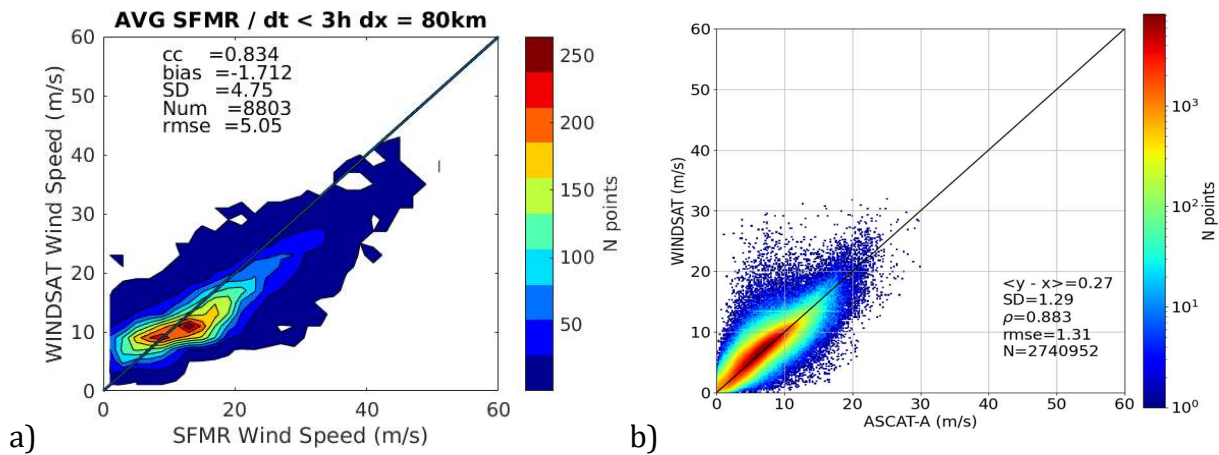


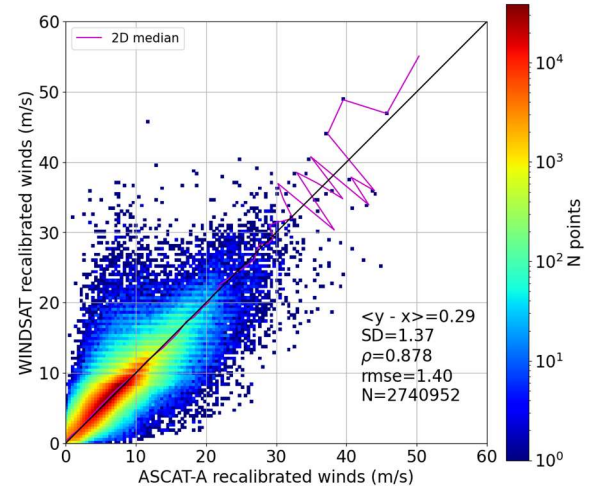
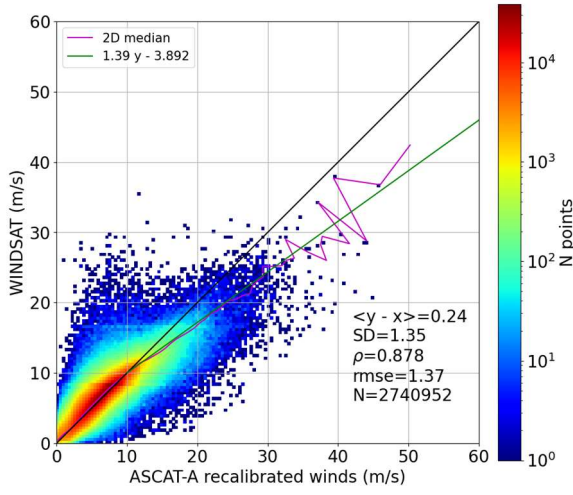
Figure 27. Contourplots of Windsat winds (only wind data for rain below 12 mm/h) versus collocated SFMR 80-km averaged winds (a) and ASCAT-A winds (b). Only collocations with $\Delta t \leq 3$ h are considered. The same statistical parameters as in Figure 8 can be found in the legend.

As for AMSR-2, to ensure good inter-calibration between ASCAT recalibrated and Windsat winds, a recalibration of Windsat moderate and high winds is proposed in Figure 28. Moreover, the recalibration function is tuned to optimize the fit to both the ASCAT recalibrated winds under non-TC conditions up to 20-25 m/s (Figure 28a) and the SFMR extreme (above 20-25 m/s) winds (Figure 27a). The resulting 1st order polynomial fit (see green curve in Figure 28a) is expressed as follows:

$$U_{10s}^* = 1.39U_{10s} - 3.892; \forall U_{10s} > 10 \text{ m/s} \quad (5)$$

Where U_{10s} and U_{10s}^* represent the Windsat original and recalibrated wind speed, respectively.

Figure 28b shows indeed good inter-calibration between Windsat recalibrated winds (using Eq. 5) and ASCAT-A recalibrated winds (using Eq. 2). Figure 29 shows the AMSR-2 recalibrated winds against collocated SFMR winds. In comparison with Windsat original winds (Figure 27a), the recalibrated winds show a substantially better alignment with SFMR winds above 20 m/s. However, the already mentioned anomalous behavior of Windsat original winds (for SFMR winds in the range 10-20 m/s) remains after recalibration. As for AMSR-2, this anomalous behavior is only found under TC conditions and therefore needs further investigation.



a)

b)

Figure 28. (a) Contourplot of Windsat winds (only wind data for rain below 12 mm/h) versus ASCAT-A recalibrated winds, together with the median curve (purple) and the polynomial function fit (green) superimposed; (b) contourplot of Windsat recalibrated winds versus ASCAT-A recalibrated winds, together with the median curve (purple). Only collocations with $\Delta t \leq 3$ h are considered. The Windsat recalibration function is shown in Eq. 5. The same statistical parameters as in Figure 8 can be found in the legend.

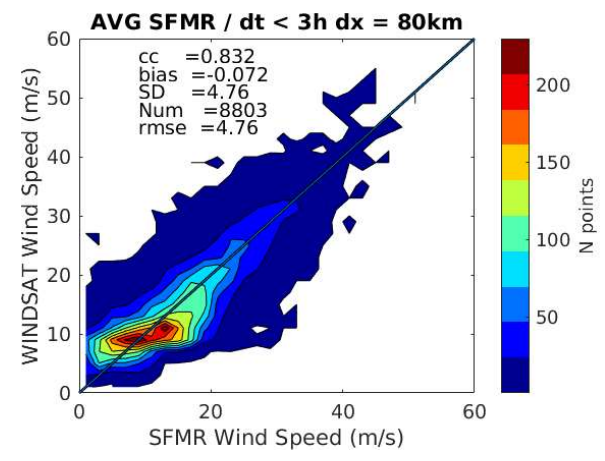


Figure 29. Contourplot of Windsat recalibrated winds versus collocated SFMR 80-km averaged winds. Only collocations with $\Delta t \leq 3$ h are considered. The Windsat recalibration function is shown in Eq. 5. The same statistical parameters as in Figure 8 can be found in the legend.

7.3 SMAP

Figure 30 shows SMAP winds versus collocated SFMR 80-km averaged winds (a) and ASCAT-A winds (b). While the entire SMAP data record is used in Figure 30a (04/2015-12/2020), a shorter period of 6 months is used in Figure 30b (05/2016-10/2016). Note that SMAP winds slightly underestimate (overestimate) SFMR winds in the range 20-30 m/s (above 30 m/s), while they clearly overestimate ASCAT-A winds above 15 m/s. In contrast, SMAP winds underestimate ASCAT-A recalibrated winds in the range 15-30 m/s (Figure 31a).

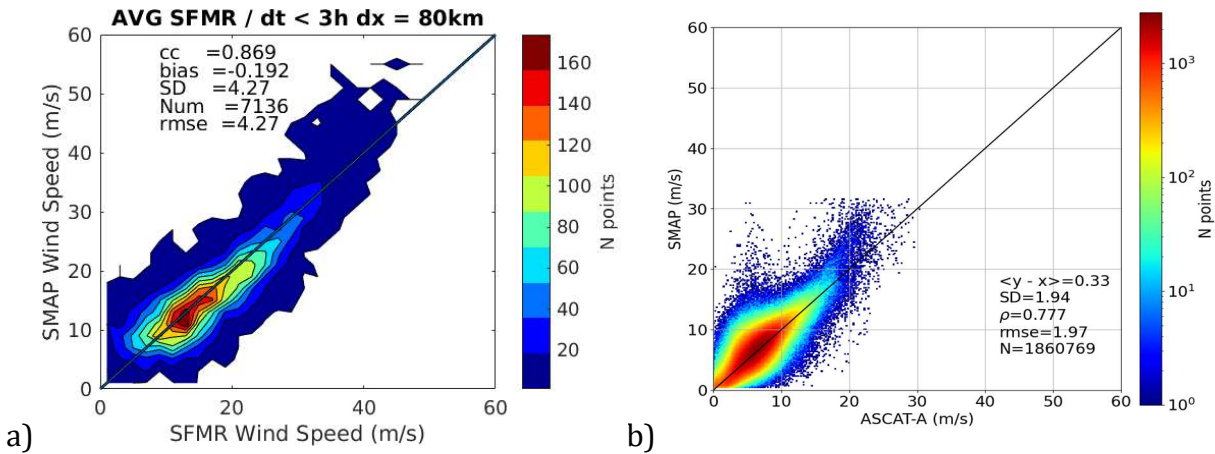


Figure 30. Contourplots of SMAP winds versus collocated SFMR 80-km averaged winds (a) and ASCAT-A winds (b). Only collocations with $\Delta t \leq 3$ h are considered. The same statistical parameters as in Figure 8 can be found in the legend.

A similar strategy to that of Windsat is followed for SMAP, such that the recalibration function ensures a fair inter-calibration with both the SFMR (Figure 30a) and the ASCAT-A recalibrated (Figure 31a) winds. The resulting 2nd order polynomial fit (see green curve in Figure 31a) is expressed as follows:

$$U_{10s}^* = -0.007844U_{10s}^2 + 1.355U_{10s} - 3.284; \forall U_{10s} > 13 \text{ m/s} \quad (6)$$

Where U_{10s} and U_{10s}^* represent the SMAP original and recalibrated wind speed, respectively.

Figure 31b shows a residual underestimation of SMAP recalibrated winds with respect to ASCAT recalibrated winds, in the range 15-22 m/s. This residual effect is caused by the fact that the recalibration function fit favours a good inter-calibration of SMAP and SFMR extreme winds, as seen in Figure 32, over the SMAP/ASCAT-A inter-calibration. A two step function could have been chosen in order to optimize SMAP inter-calibration with both ASCAT-A recalibrated and SFMR winds, but this has been discarded to avoid discontinuities in the wind field which can cause artifacts in the, e.g., wind derivatives. Moreover, the selected

recalibration function (Eq. 6) generally leads to a good inter-calibration of SMAP, ASCAT-A (recalibrated), and SFMR winds.

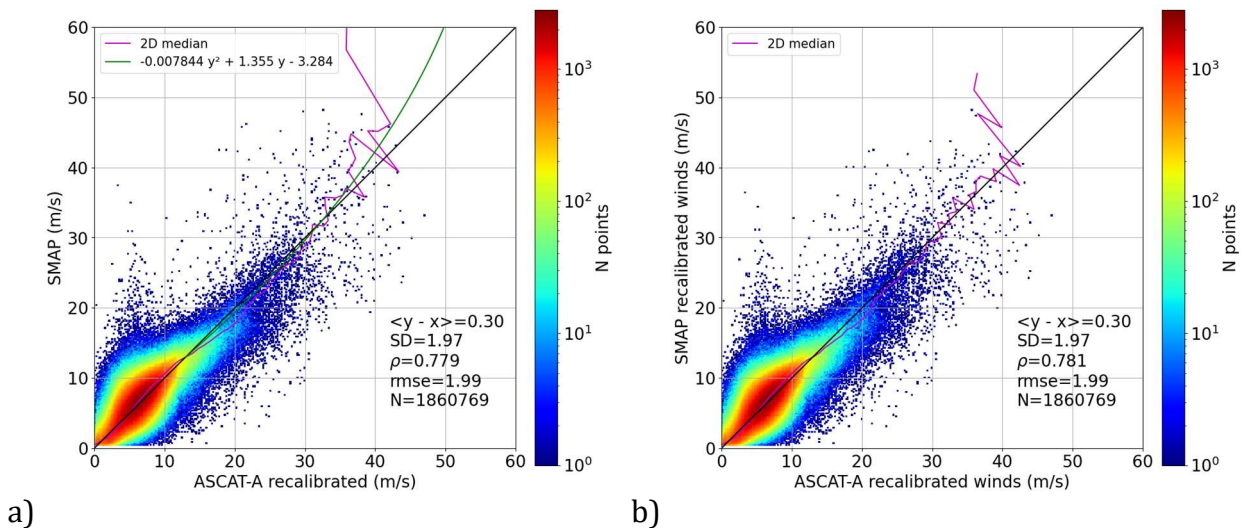


Figure 31. (a) Contourplot of SMAP winds versus ASCAT-A recalibrated winds, together with the median curve (purple) and the polynomial function fit (green) superimposed; (b) contourplot of SMAP recalibrated winds versus ASCAT-A recalibrated winds (b), together with the median curve (purple) Only collocations with $\Delta t \leq 3$ h are considered. The SMAP recalibration function is shown in Eq. 6. The same statistical parameters as in Figure 8 can be found in the legend.

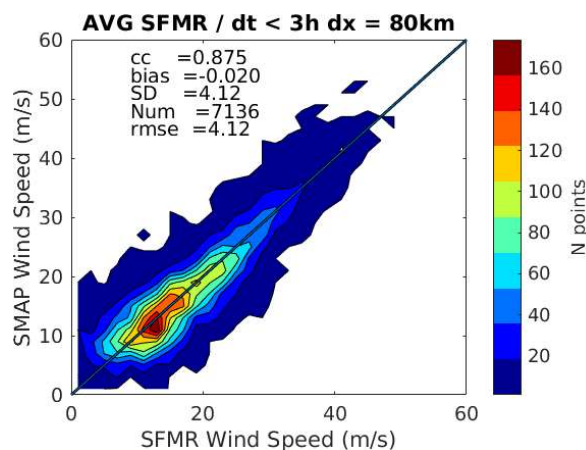


Figure 32. Contourplot of SMAP recalibrated winds versus collocated SFMR 80-km averaged winds. Only collocations with $\Delta t \leq 3$ h are considered. The SMAP recalibration function is shown in Eq. 6. The same statistical parameters as in Figure 8 can be found in the legend.

7.4 SMOS

Figure 33 shows SMOS winds versus collocated SFMR 80-km averaged winds (a) and ASCAT-A winds (b). While the entire SMAP data record is used in Figure 33a (01/2010-12/2020), a shorter period of 6 months is used in Figure 33b (05/2016-10/2016). Note that in general, SMOS winds are more noisy than SMAP winds (see the larger scatter in Figure 33a than in Figure 30a). However, as seen in Figure 33a, SMOS winds are well aligned (well inter-calibrated) with SFMR very high and extreme winds, i.e., above 20 m/s. Below 20 m/s, SMOS winds slightly underestimate SFMR winds, while they present a good alignment with ASCAT-A winds (Figure 33b). In turn, SMOS winds do underestimate ASCAT-A recalibrated winds in the range 12-20 m/s (Figure 34a).

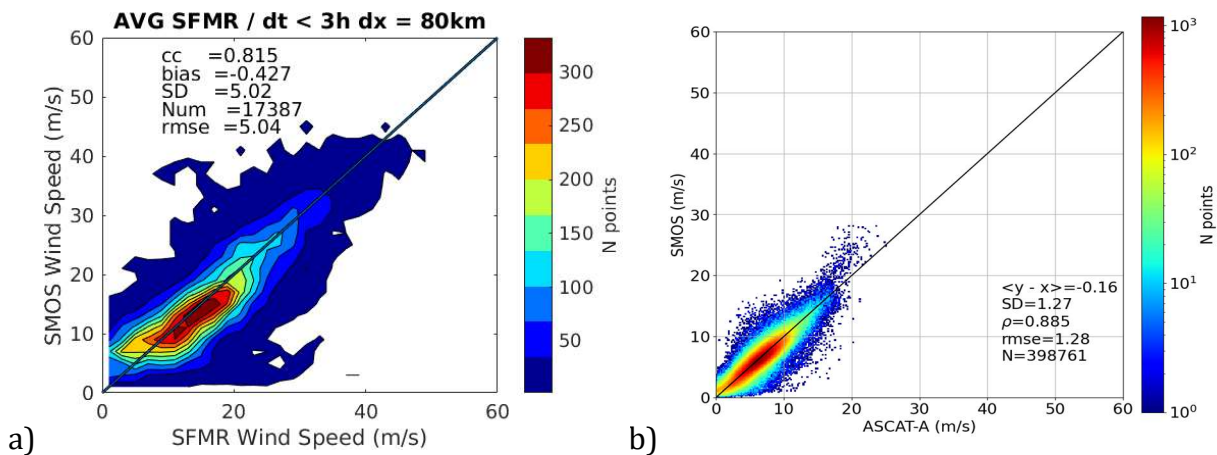


Figure 33. Contourplots of SMOS winds versus collocated SFMR 80-km averaged winds (a) and ASCAT-A winds (b). Only collocations with $\Delta t \leq 3$ h are considered. The same statistical parameters as in Figure 8 can be found in the legend.

A similar strategy to that of the other radiometers is followed for SMOS, such that the recalibration function ensures a fair inter-calibration with both the SFMR (Figure 33a) and the ASCAT-A recalibrated (Figure 34a) winds. The resulting 3rd order polynomial fit (see green curve in Figure 34a) is expressed as follows:

$$U_{10s}^* = 0.002452U_{10s}^3 - 0.1678U_{10s}^2 + 4.486U_{10s} - 21.9; \forall U_{10s} \in [12, 20.5] \text{ m/s} \quad (7)$$

Where U_{10} and U_{10}^* represent the SMAP original and recalibrated wind speed, respectively.

Similar to SMAP recalibration, Figure 34b shows a residual underestimation of SMOS recalibrated winds with respect to ASCAT recalibrated winds, in the range 15-20 m/s. Again, this residual effect is caused by the fact that the recalibration function fit favours good inter-calibration of SMOS and SFMR extreme winds, as seen in Figure 35. In fact, Eq. 7 does not

modify SMOS winds above 20 m/s, since they are already well aligned with SFMR in this range (see Figure 33a). It modifies though SMOS winds in the range 12-20 m/s, leading to better agreement between SMOS and SFMR winds after recalibration (see Figures 33a and 35). As such, the selected recalibration function (Eq. 7) generally leads to a good inter-calibration of SMOS, ASCAT-A (recalibrated), and SFMR winds.

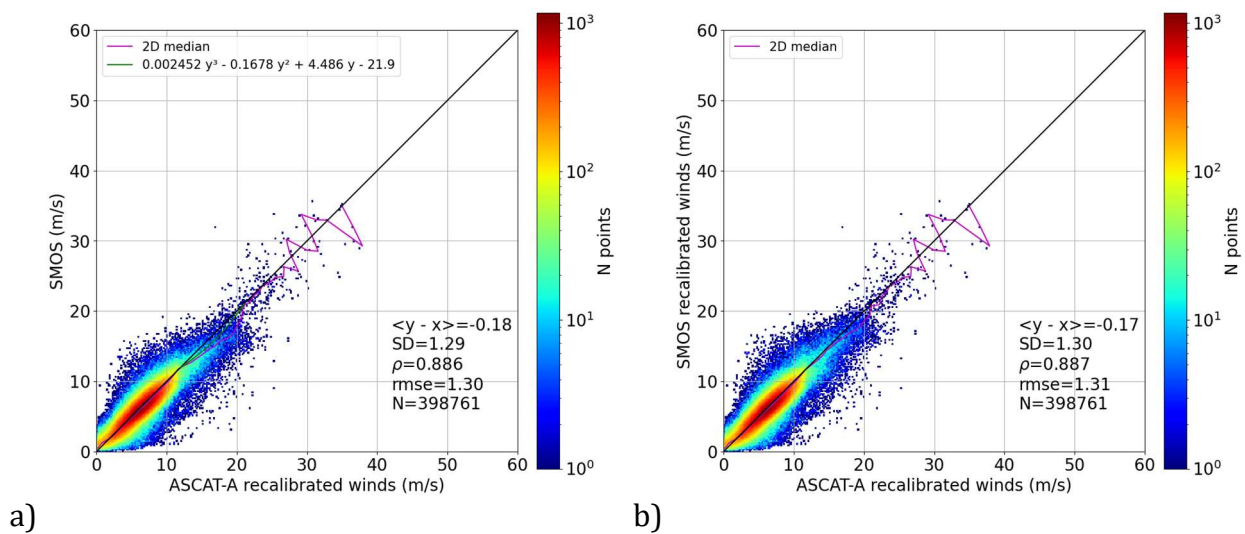


Figure 34. Contourplot of SMOS winds versus ASCAT-A recalibrated winds (a), together with the median curve (purple) and the polynomial function fit (green) superimposed. Contourplot of SMOS recalibrated winds versus ASCAT-A recalibrated winds (b), together with the median curve (purple) Only collocations with $\Delta t \leq 3$ h are considered. The SMOS recalibration function is shown in Eq. 7. The same statistical parameters as in Figure 8 can be found in the legend.

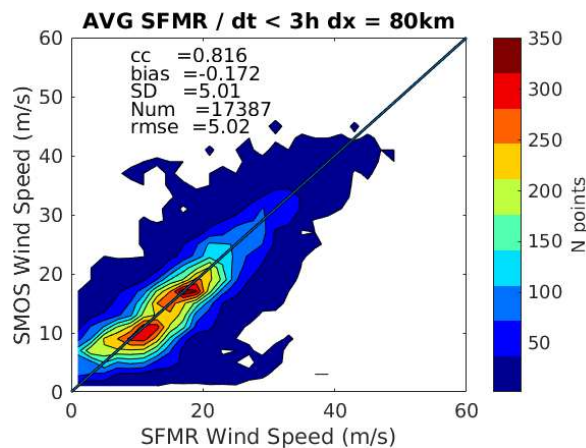


Figure 35. Contourplot of SMOS recalibrated winds versus collocated SFMR 80-km averaged winds. Only collocations with $\Delta t \leq 3$ h are considered. The SMOS recalibration function is shown in Eq. 7. The same statistical parameters as in Figure 8 can be found in the legend.

In summary, a two-step strategy has been followed to recalibrate the high and extreme wind speeds derived from the vast majority of satellite, swath-based, medium resolution active (scatterometers) and passive (radiometers) microwave systems available in the period 2009-2020. First, the C-band ASCATs have been recalibrated against collocated storm-motion centric SFMR wind data. Then, both SFMR winds and ASCAT recalibrated winds have been used to recalibrate all the other satellite wind systems. In doing so, a good inter-calibration between all the systems is ensured not only under TC conditions, but also elsewhere. Small residual biases are present in the 15-20 m/s range of SMAP and SMOS recalibrated winds, under nominal (non TC) conditions. Both AMSR-2 and Windsat winds show an anomalous behavior in the range 10-20 m/s under TC conditions that deserves further investigation. Finally, it is found that Ku-band extreme winds (i.e., close to the hurricane eyewall region) are substantially impacted by rain contamination, leading to underestimation of such winds. It is therefore recommended to use the KNMI_QC and VAR_QC flags to filter out such WVCs. Note that current improvements in Ku-band rain correction [Xu and Stoffelen, 2021] and flagging [Xu and Stoffelen, 2020] may lead to improved extreme wind sampling of Ku-Band systems in the near future.

8 REFERENCES

- [De Kloe et al., 2017] De Kloe J., Stoffelen A. and Verhoef A., "Improved Use of Scatterometer Measurements by Using Stress-Equivalent Reference Winds," *IEEE J. of Selected Topics in Applied Earth Observations and Remote Sensing*, vol. 10, no. 5, pp. 2340-2347, 2017.
- [Knapp et al., 2010] K.R. Knapp, M.C. Kruk, D.H. Levinson, H. J. Diamond, and C. J. Neumann, "The International Best Track Archive for Climate Stewardship (IBTrACS): Unifying tropical cyclone best track data", *Bulletin of the American Meteorological Society*, vol. 91, pp. 363-376, 2010.
- [Klotz and Uhlhorn, 2014] B. Klotz and E. Uhlhorn, "Improved Stepped Frequency Microwave Radiometer Tropical Cyclone Surface Winds in Heavy Precipitation", *J. Atmos. Ocean. Technol.*, vol. 31, p. 2392-2408, 2014.
- [Lin and Portabella, 2017] W. Lin, and M. Portabella, "Towards an improved wind quality control for RapidScat," *IEEE Trans. Geosci. Rem. Sens.*, 55 (7), pp. 3922-3930, 2017.

- [Lin et al., 2015] W. Lin, M. Portabella, A. Stoffelen, A. Verhoef, and A. Turiel, "ASCAT wind quality control near rain," *IEEE Trans. Geosci. Rem. Sens.*, 53 (8), pp. 4165-4177, 2015.
- [Meissner et al., 2021] Meissner, T.; Ricciardulli, L.; Manaster, A., "Tropical Cyclone Wind Speeds from WindSat, AMSR and SMAP: Algorithm Development and Testing," *Remote Sens.*, 13, 1641, 2021.
- [Manaster et al., 2021] Manaster, A.; Ricciardulli, L.; Meissner, T., "Tropical Cyclone Winds from WindSat, AMSR2, and SMAP: Comparison with the HWRP Model, *Remote Sens.*, 13, 2347, 2021.
- [Polverari et al., 2022] Polverari, F., Portabella, M., Lin, W., Sapp, J.W., Stoffelen, A., Jelenak, Z., and Chang, P.S., "On High and Extreme Wind Calibration Using ASCAT," *IEEE Trans. Geosci. Rem. Sens.*, 60, <https://doi.org/10.1109/TGRS.2021.3079898>, 2022.
- [Portabella et al., 2012] M. Portabella, A. Stoffelen, A. Verhoef, and J. Verspeek, "A new method for improving scatterometer wind quality control," *IEEE Geosci. Rem. Sens. Lett.*, 9 (4), pp. 579-583, 2012.
- [Portabella and Stoffelen, 2001] M. Portabella and A. Stoffelen, "Rain detection and quality control of SeaWinds," *J. Atm. and Ocean Techn.*, 18 (7), pp. 1171-1183, 2001.
- [Reul et al., 2017] Reul, N., B. Chapron, E. Zabolotskikh, C. Donlon, A. Mouche, J. Tenerelli, F. Collard, J.F. Piolle, A. Fore, S. Yueh, J. Cotton, P. Francis, Y. Quilfen, and V. Kudryavtsev, "A new generation of tropical cyclone size measurements from space," *Bull. Amer. Meteor. Soc.*, 98, 2367-2385, doi:10.1175/BAMS-D-15-00291.1, 2017.
- [Sapp et al., 2019] J.W. Sapp, S.O. Alswiss, Z. Jelenak, P.S. Chang, J. Carswell, "Stepped Frequency Microwave Radiometer Wind-Speed Retrieval Improvements", *Remote Sensing*, vol. 11, no. 214, 2019.
- [Stoffelen et al., 2020] Stoffelen, A., Mouche, A., Polverari, F., Van Zadelhoff, G.-J., Sapp, J., Portabella, M., Chang, P., Lin, W., and Jelenak, Z., "C-band High and Extreme-Force Speeds (CHEFS)," *Final report EUMETSAT ITT 16/166*, April 2020.
- [Stoffelen et al., 2017] Stoffelen, A., J. Verspeek, J. Vogelzang and A. Verhoef, "The CMOD7 Geophysical Model Function for ASCAT and ERS Wind Retrievals," *IEEE J. Sel. Topics in Appl. Earth Obs. And Rem. Sens.* 10 (5), 2123-2134, doi:10.1109/JSTARS.2017.2681806, 2017.
- [Verhoef et al., 2017] Verhoef, A., J. Vogelzang, J. Verspeek and A. Stoffelen, "Long-Term Scatterometer Wind Climate Data Records," *IEEE J. Sel. Top. Appl. Earth Obs. Remote Sens.*, 2017, 10, 5, 2186-2194, doi:10.1109/JSTARS.2016.2615873.
- [Vogelzang, 2017] J. Vogelzang, "Two dimensional variational ambiguity removal (2DVAR)," *KNMI Tech. Note NWP SAF NWPSAF-KN-TR-004*, 2017.

[Xu and Stoffelen, 2020] X. Xu and A. Stoffelen, "Improved rain screening for ku-band wind scatterometry," *IEEE Trans. Geosci. Remote Sens.*, 58 (4), pp. 2494–2503, 2020.

[Xu and Stoffelen, 2021] X. Xu and A. Stoffelen, "Support vector machine tropical wind speed retrieval in the presence of rain for Ku-band wind scatterometry," *Atmos. Meas. Tech.*, 14, 7435–7451, 2021.

[Wange et al., 2017] Wang, Z. et al., "SST Dependence of Ku- and C-Band Backscatter Measurements," *IEEE Journal of Selected Topics in Applied Earth O*, 10, 5, 2135-2146, doi:10.1109/JSTARS.2016.2600749, 2017.